Thermodynamics of Oiling-Out in Antisolvent Crystallization. II. Diffusion toward Spinodal Decomposition

Zhengyu Zhang, Jean-Frédéric Audibert, Weixi Wang, Valérie Génot, Soo Young Park, Anne Spasojević-de Biré, Robert Pansu

Thermodynamics of Oiling-Out in Antisolvent Crystallization.

II. Diffusion toward Spinodal Decomposition

Zhengyu Zhang[1,2,3*], Jean-Frédéric Audibert[3,4], Weixi Wang[5], Valérie Génot[6], Soo Young Park[7], Anne Spasojević-de Biré[1], Robert B. Pansu[2,3]

[1] Université Paris-Saclay, CentraleSupélec, CNRS, Laboratoire SPMS, 91190 Gif-sur-Yvette, France

[2] Université Paris-Saclay, CNRS, Ecole Normale Supérieure Paris-Saclay, CentraleSupélec, Laboratoire LuMIn, 91190 Gif-sur-Yvette, France

[3] Université Paris Saclay, Institut d'Alembert (IDA), CNRS, Ecole Normale Supérieure Paris-Saclay, 91190 Gif-sur-Yvette, France

[4] Université Paris-Saclay, CNRS, Ecole Normale Supérieure Paris-Saclay, Laboratoire PPSM, 91190 Gif-sur-Yvette, France

[5] École polytechnique, LPICM, CNRS, Institut Polytechnique de Paris, 91120 Palaiseau, France

[6] IUT d'Orsay, Université Paris Saclay, 91190 Gif-sur-Yvette, France

[7] Department of Materials Science and Engineering, Seoul National University, 1 Gwanak-ro, Gwanak-gu, Seoul 151-744, Korea

*Correspond to: zhengyu.zhang@centralesupelec.fr

Highlights

- Time-dependent simulation of antisolvent-induced solute uphill diffusion and spinodal decomposition.
- Microfluidic observation of the simulation-predicted phenomena.
- Diffusion trajectories on phase diagram unveil thermodynamic conditions prior to phase transitions.
- Effect of control parameters investigated: antisolvent mitigation by good solvent, solute concentration, antisolvent-to-solution size ratio, and agitation shear rate.
- Analysis of rate of entropy production and drag forces.

For journal front art

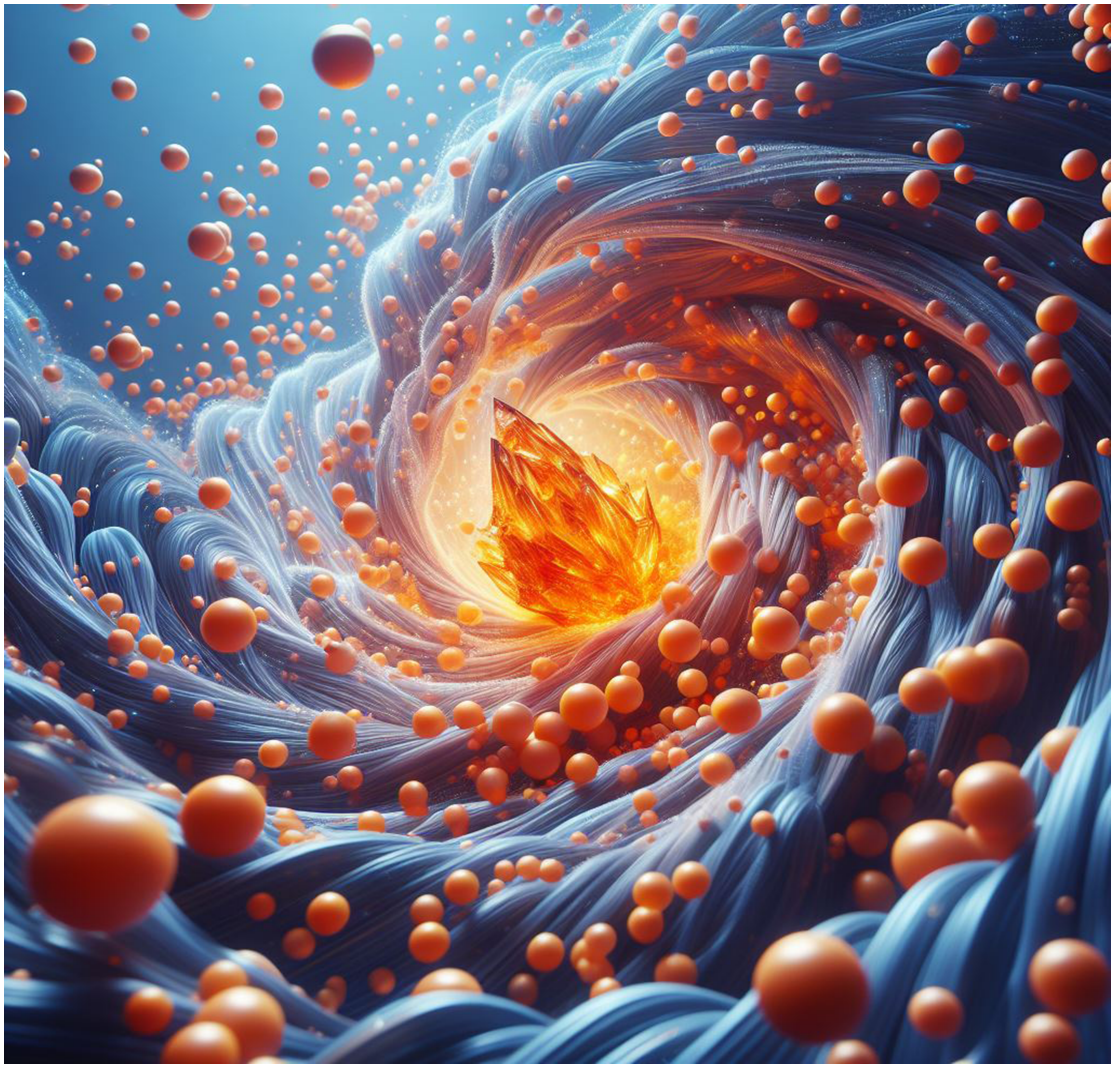

From chaos to order: the influx of antisolvent raises the solute energy level. This energy wave drives solute molecules to focus, ultimately inducing phase transitions. (Artwork generated using *DALL·E 3*)

TOC Graphic

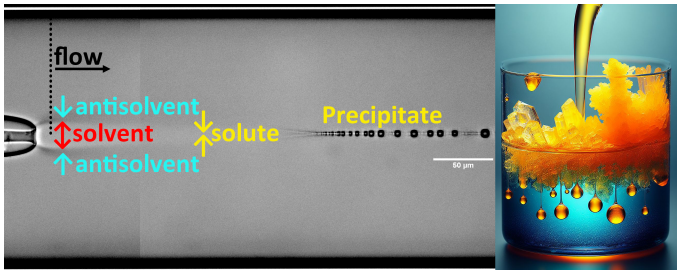

Synopsis

The antisolvent influx raises the solute energy. This energy wave focuses the solute, leading to the competition between crystallization and oiling-out. Time-dependent simulations reveal that the strength of the focusing effect increases with the magnitude, scale, and agitation of the antisolvent gradient. Characteristic times of oiling-out and two sites for antisolvent-induced spinodal decomposition are identified by simulations and microfluidics.

Keywords

Antisolvent crystallization; Oiling-out; Spinodal decomposition; Microfluidics; multicomponent diffusion simulation; Fluorescence

Abstract

The extensive use of antisolvent crystallization for poorly soluble chemicals is hindered by oiling-out. Part I explored the thermodynamics of oiling-out in antisolvent crystallization of an organic solute with aqueous-organic cosolvents. This sequel investigates the diffusion kinetics upon antisolvent addition. We conduct time-dependent simulations on a hypothetical micrometric diffusion couple, with chemical potential gradients being the driving forces within the Maxwell-Stefan model. Diffusion trajectories on the phase diagram unveils the thermodynamic conditions before phase transitions. Computational results show that the influx of antisolvent raises the solute energy level. This energy wave drives the solute to focus toward the good solvent. Antisolvent gradient dominates the strength of the focusing effect. Initial solute concentration acts as an offset in diffusion trajectories. Antisolvent-to-solution size ratio determines the characteristic time of the antisolvent focusing. Agitation in antisolvent enhances the focusing effect over extended diffusion time. The solute accumulation leads to crystallization or oiling-out. Microfluidics and simulations demonstrate characteristic times of oiling-out and two sites of occurrence for antisolvent-induced spinodal decomposition. We bring a unified methodology, from solubility to irreversible thermodynamics, to address the competition between antisolvent crystallization and oiling-out. The methodology and insights can be applied to other antisolvent crystallization systems.

Abbreviations

ASC	antisolvent crystallization
ASP	antisolvent precipitation
DBDCS	(2*Z*,2'*Z*)-2,2'-(1,4-phenylene)bis(3-(4-butoxyphenyl) acrylonitrile)
G-x	Gibbs energy, *G*, as a function of amount fraction composition, x
LAS	liquid antisolvent
LLE	liquid-liquid equilibrium
LLPS	liquid-liquid phase separation
M-S	Maxwell-Stefan model
SLE	solid-liquid equilibrium
VLE	vapor-liquid equilibrium

Nomenclatures

Notation	Definition	Unit
c	amount concentration	$mol^{-1} \cdot m^{-3}$
d	distance	m
D	Fick diffusion coefficient	$m^2 \cdot s^{-1}$
$Đ$	Maxwell-Stefan diffusivity	$m^2 \cdot s^{-1}$
f	drag force	N
F	driving force per mole	$N \cdot mol^{-1}$
G	Gibbs energy	J
J	molar flux with respect to the mean-molar reference frame	$mol \cdot m^{-2} \cdot s^{-1}$
k_B	Boltzmann constant, ~1.381×10^{-23} $J \cdot K^{-1}$	$J \cdot K^{-1}$
L	size of antisolvent	m
n	number of components	1
N_A	Avogadro constant, ~$6.022 \times 10^{23} mol^{-1}$	mol^{-1}
Pe	Péclet number	1
Q	flow rate	$m^3 \cdot s^{-1}$
r	radius	m
R	gas constant, ~8.314 $J \cdot mol^{-1} \cdot K^{-1}$	$J \cdot K^{-1} mol^{-1}$
R	size of solution	m
Re	Reynolds number	1
$S_{\%}$	supersaturation ratio	1
t	time	s
T	absolute temperature	K
u	diffusion velocity	$m \cdot s^{-1}$
v	convection velocity	$m \cdot s^{-1}$
x	amount fraction	1
z	spatial coordinate	m
γ	shear rate	s^{-1}
η	dynamic viscosity	Pa·s
λ	activity coefficient	1
μ	chemical potential	$J \cdot mol^{-1}$
ρ	mass concentration, mass density	$kg \cdot m^{-3}$
σ	rate of entropy production per unit volume	$J \cdot K^{-1} \cdot m^{-3} \cdot s^{-1}$
ϕ	volume fraction	1

Super- and sub-scripts	
c	property of central flow
diff	property associated with diffusion
i	property of component i

ij	property of *i-j*
$i(j)$	property of component i in j
L	property of left side of diffusion couple
max	maximum
R	property of right side of diffusion couple
p	property of peripheral flow
r	property at ambient temperature
0	zero
*	self, tracer
*	property at a critical time or condition

1. Introduction

The liquid antisolvent (LAS) process is a separation technique widely utilized in the chemical industry. Its process design entails selecting a pair of miscible aqueous-organic cosolvents, with the solute exhibiting higher solubility in one solvent than in the other. Supersaturation is controlled by introducing the non-solvent into the solution. It induces either liquid precipitation (antisolvent precipitation, ASP) or crystallization (antisolvent crystallization, ASC). A two-step[1, 2] crystallization can also occur through a transient liquid precipitation, known as "oiling-out"[3, 4].

Antisolvent-induced spontaneous emulsification of liquid droplets has been coined the "ouzo effect"[5] after an anise-flavored Mediterranean spirit, which is customarily consumed as a milky emulsion by mixing with water. This effect yields a metastable emulsion without requiring mechanical shear[6] or surfactant[7]. It is a complex phenomenon involving factors such as solubility in cosolvents, non-ideal multicomponent diffusion, and surface tension dynamics. Recent simulations[8, 9] reveal that, even with the initial and the fully mixed compositions below the liquid-liquid equilibrium (LLE), local compositions can transiently surpass the LLE, through "serpentine"[8] diffusion trajectories, resulting in liquid-liquid phase separation (LLPS).

In oiling-out scenarios, the solid-liquid equilibrium (SLE) concentration falls below the metastable LLE. ASC occurs under moderate antisolvent addition, such as by a slow rate of addition or a mélange of cosolvents. However, minuscule solubility in the antisolvent easily leads to high supersaturation upon antisolvent addition, thus facilitating the formation of amorphous precipitates[10] and metastable polymorphs[11, 12]. Oiling-out adversely affects crystallization quality and efficiency, posing a significant challenge in crystallization process design.[13, 14] Conversely, producing micro-/nano-particles and metastable phases offers a strategy for enhancing the bioavailability of pharmaceutical ingredients.[15, 16] These industrial demands have spurred extensive interest[17, 18, 19] in investigating the competition between oiling-out and crystallization. While multicomponent diffusion in ASP has been investigated by Krishna[8, 9], numerical simulations of solute uphill diffusion in ASC has only recently been

explored[20, 21], despite the resurgent interest. This might be due to a lack of thermodynamic data on solute-solvent binary systems.

In Part I[2], we provided a comprehensive thermodynamic description of oiling-out in antisolvent crystallization of a poorly-soluble organic solute in aqueous-organic cosolvents. The example solute, DBDCS (cf. **Figure 1**), is a fluorophore exhibiting aggregation-induced emission. Its fluorescence lifetime and the quantum yield increase after aggregation[22, 23], allowing for detection of fluorescent crystal nucleation and growth against a non-fluorescent background.[24, 20] DBDCS is insoluble in water (the non-solvent) and slightly soluble in 1,4-dioxane (the "good" solvent, solubility 8 g/L).[2] Two polymorphs of DBDCS have been reported to switch under shear stress: the γ phase (green emission, fluorescence lifetime > 10 ns) and the β phase (blue emission, fluorescence lifetime < 6 ns).[22, 20] The Jouyban-Acree model[25, 26] allows us to extract thermodynamic parameters from solubility measurement. We constructed a ternary phase diagram by calculating the spinodal decomposition limit, metastable LLE, polymorph SLE, and chemical potentials of each component. The computational results matched the phase diagram measured through microfluidics. By analyzing energy gains of composition fluctuations, we suggested optimal conditions for crystallization, for oiling-out, and for spinodal decomposition. The phase diagram assesses the potential for establishing equilibrium but not the rate of achieving equilibrium from a non-equilibrium state.

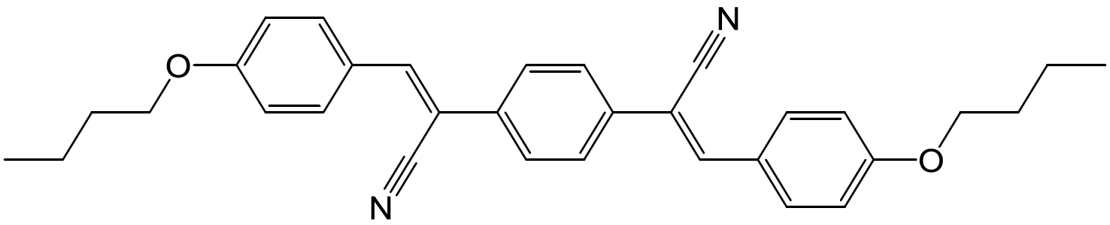

Figure 1. Molecular structure of DBDCS [(2*Z*,2'*Z*)-2,2'-(1,4-phenylene)bis(3-(4-butoxyphenyl) acrylonitrile)]. Formula: $C_{32}H_{32}N_2O_2$. Relative molecular mass: 476.60.

Moving from equilibrium to irreversible thermodynamics, this sequel explores the kinetics of molecular migrations upon antisolvent addition in the example system of water-[1,4-

dioxane]-DBDCS. With chemical potential gradients as driving forces in the framework of the Maxwell-Stefan (M-S) model[27, 9], we performed time-dependent simulation on a hypothetical micrometric diffusion couple. We systematically examine the impacts of mixing parameters: antisolvent mitigation fraction by the good solvent, initial solute concentration, antisolvent-to-solution size ratio, and shear rate of agitation. The structure of this paper includes: Section 2 introducing irreversible thermodynamics; Section 3 describing the numerical method; Section 4 presenting two sites of occurrence for antisolvent-induced spinodal decomposition; Section 5 featuring diffusion trajectories on the phase diagram; Section 6 examining the impacts of mixing parameters on the kinetics, with the entropy production rate, diffusion driving force, and characteristic time of oiling-out also addressed; Section 7 discussing the characteristic shape of the diffusion trajectories. Together, our Parts I and II bring a unified methodology, from thermodynamics to kinetics, addressing the competition between antisolvent crystallization and oiling-out. The methodology and insights from this study offer potential for parameter optimization in the process design of other antisolvent crystallization systems.

2. Irreversible thermodynamics

The origins of irreversible thermodynamics trace back to early theories on diffusion of gases[28] and liquids[29, 30]. Onsager formulated the reciprocal relation between forces and fluxes[31, 32] and addressed the problem of liquid diffusion[33]. After that, comprehensive theoretical frameworks, such as the generalized M-S formulation[34, 27, 35, 9] and the generalized Fick's law[27, 35, 36, 9], have been developed to describe non-ideal multicomponent transport under diverse force fields within classical field theory[37].

Irreversible thermodynamics is an extension of classical thermodynamics, based on several basic postulates.[27] The first is the quasi-equilibrium postulate, i.e., the departure from local equilibrium is small, allowing state functions to be defined locally as in equilibrium systems. The second is the linearity postulate, i.e., fluxes are a linear transformation of driving forces. Following Onsager's reciprocal relation[31, 32], the flux-force coefficient matrix is positive definite and symmetric[27, 8, 9]. Lastly, rate of energy dissipation is the product of force and

velocity[9, 38], and the total rate of entropy production must be non-negative, comply with the second law of thermodynamics.

2.1. Generalized Maxwell-Stefan diffusion model

In his paper on fluid dynamics[39], Stokes resolved a simplified Navier-Stokes equation[40, 41] for a spherical particle in creeping flow and derived a linear relation between the drag and velocity:

$$-f = 6\pi r\eta u\,, \tag{1}$$

where f is the drag on the sphere, r its radius, η the dynamic viscosity of the medium, and u the velocity of the sphere relative to the medium. Einstein later referenced to this relation in his theoretical paper[42] on Brownian motion, where he got the drag coefficient

$$6\pi r\eta = \frac{RT}{N_{\mathrm{A}}D} \tag{2}$$

with R the gas constant, T the absolute temperature, N_{A} the Avogadro constant, and D the diffusion coefficient. Einstein's equation was experimentally validated by Perrin[43], whereby he measured N_{A} and evidenced the existence of molecules.

The diffusion coefficient for a species infinitely diluted in a homogeneous medium can be described by eq. 2. What about a non-homogeneous medium with multiple components intermingling? The M-S diffusion model, developed in parallel by Maxwell[28] for gases and by Stefan[30] for liquids, posits that the force on a species *i* is balanced by the sum of the frictions between *i* and all other species:

$$F_i = \sum_{j=1}^{n} \frac{RT}{Đ_{ij}} x_j\left(u_i - u_j\right)\,, \tag{3}$$

where, analogous to eq. 1, F_i is the force on component *i* per mole, $RT/Đ_{ij}$ the drag coefficient between fluxes i and j, x_j the amount fraction of component j, $u_i - u_j$ is the velocity of

component i relative to flux j, and n is the number of components in the mixture. This is the dominant theory on non-ideal multicomponent diffusion.[9]

Our study considers isothermal, isobaric processes in the absence of external force fields. The driving force exerted on species i by its chemical potential gradient is

$$F_i = -\frac{\mathrm{d}\mu_i}{\mathrm{d}z} \tag{4}$$

where μ_i is the chemical potential of component i, and z the spatial coordinate. In scenarios with external force fields, driving forces may include gravity, centrifugal force, electric potential gradient, optical gradient force, temperature gradient, and so on.[34, 27]

2.2. Maxwell-Stefan diffusivities

M-S diffusivities, representing pairwise intermolecular frictions, are composition dependent. A challenge in nonideal multicomponent liquid diffusion is that multicomponent diffusivity data are rarely available. The values of M-S diffusivities still rely on molecular dynamic simulations[44, 45, 46, 47] and empirical relations[48, 49, 50, 9], such as the Darken-type equations[51, 44] and the Vignes-type relations[52, 53, 44]. The Darken equation[51, 54] is widely used to describe mutual diffusion coefficients in binary mixtures (cf. Section S6), considering both hydrodynamics and thermodynamics. The hydrodynamic part of the Darken equation has been extrapolated to multicomponent systems for estimating M-S diffusivities:[44, 45, 49]

$$Đ_{ij} = \frac{x_j D_i^* + x_i D_j^*}{x_i + x_j} \ , \tag{5}$$

where $Đ_{ij}$ is the M-S diffusivity between components i and j, and D_i^* the self-diffusion coefficient[55] of component i as a function of composition.

Estimating M-S diffusivities with eq. 5 requires the self-diffusion coefficients of each component as a function of composition. Assuming that molecule sizes are composition independent, Stokes and Einstein's equations (eq. 1 and eq. 2) relate the self-diffusion coefficients to the viscosity of the medium:[56, 54]

$$D_i^* = \frac{\eta_j}{\eta} D_{i(j)}^* = \frac{\eta_j}{\eta} D_{ij(j)} \ , \tag{6}$$

where η denotes the dynamic viscosity of the mixture, η_i the dynamic viscosity of neat liquid *i*, and $D_{i(j)}^*$ the self-diffusion coefficient of component *i* at infinite dilution in liquid *j*, which is equivalent to $D_{ij(j)}$, the limiting mutual Fick diffusion coefficient at infinite dilution of *i*. Data on mutual Fick diffusion coefficients and viscosities are readily available for aqueous-organic cosolvents, not the solute. For the solute, say component *k*, its self-diffusion coefficient is estimated resorting to the Stokes-Einstein equation [42, 57, 43] (eq. 2):

$$D_k^* = \frac{k_\mathrm{B} T}{6\pi r_k \eta} \ . \tag{7}$$

where k_B is the Boltzmann constant, r_k is the Stokes-Einstein (effective) radius of a monomer of solute *k*.

2.3. Entropy production rate

The energy dissipation in non-equilibrium processes is the product of force and velocity[9, 38]. The rate of entropy production per unit volume due to the diffusion of component *i* is[31, 9]

$$\sigma_{i,\mathrm{diff}} = \frac{F_i J_i}{T} = -\frac{1}{T} \frac{\mathrm{d}\mu_i}{\mathrm{d}z} J_i \ , \tag{8}$$

where J_i denotes the molar flux of *i* with respect to the mean-molar reference frame. According to the second law of thermodynamics, the total entropy production $\sum \sigma_i \geq 0$. It remains possible for a local entropy production to be negative. A negative $\sigma_{i,\mathrm{diff}}$ suggests that the drag between flux *i* and other fluxes be stronger than the thermodynamic driving force (and the external force fields). This local consumption of entropy must be annihilated by a much faster overall entropy production.

3. Methodology

This study explores the molecular migration kinetics upon antisolvent addition in the example ternary system of water (component 1)-[1,4-dioxane] (component 2)-DBDCS (component 3) at $T_\mathrm{r} \equiv 298.15$ K and 1 atm. In our microfluidic experiment[24, 20, 2] for nucleation detection via fluorescence, DBDCS (3) dissolved in 1,4-dioxane (2) was coaxially injected into a peripheral flow of water (1) mitigated by 1,4-dioxane (2). The radius of the microfluidic channel was 100 μm. To isolate the impacts of mixing parameters and economize computation power, we employed a simplified hypothetical micrometric diffusion couple, cf. **Figure 2**. At time zero, t_0, two solutions—**L,** a homogeneous mixture of water (1)-[1,4-dioxane] (2), and **R**, DBDCS (3) dissolved in 1,4-dioxane (2)—are in contact within 100 μm. A linear vertical convection velocity field, v, can be overlayed to simulate agitation. Diffusion is usually negligible compared with convection in the same direction, therefore, it is only important to examine diffusion and convection orthogonal to each other. Simulation control parameters include the initial volume fraction of water (1) in **L**, $\phi_{1\mathrm{L}}$, the initial concentration of DBDCS (3) in **R**, $\rho_{3\mathrm{R}}$, the antisolvent-to-solution size ratio, **L**/**R**, and the agitation shear rate, $\gamma = (v_\mathrm{R} - v_\mathrm{L})/(\mathbf{L} + \mathbf{R})$. This simplified model captures general scenarios where antisolvent and solution contact on a micrometric scale, such as co-flows, droplets in contact, droplets dispersed in a continuous phase, liquid layers, and so on. The two ends of the diffusion couple can represent either phase boundaries or symmetric centers/axis of periodic phase distributions.

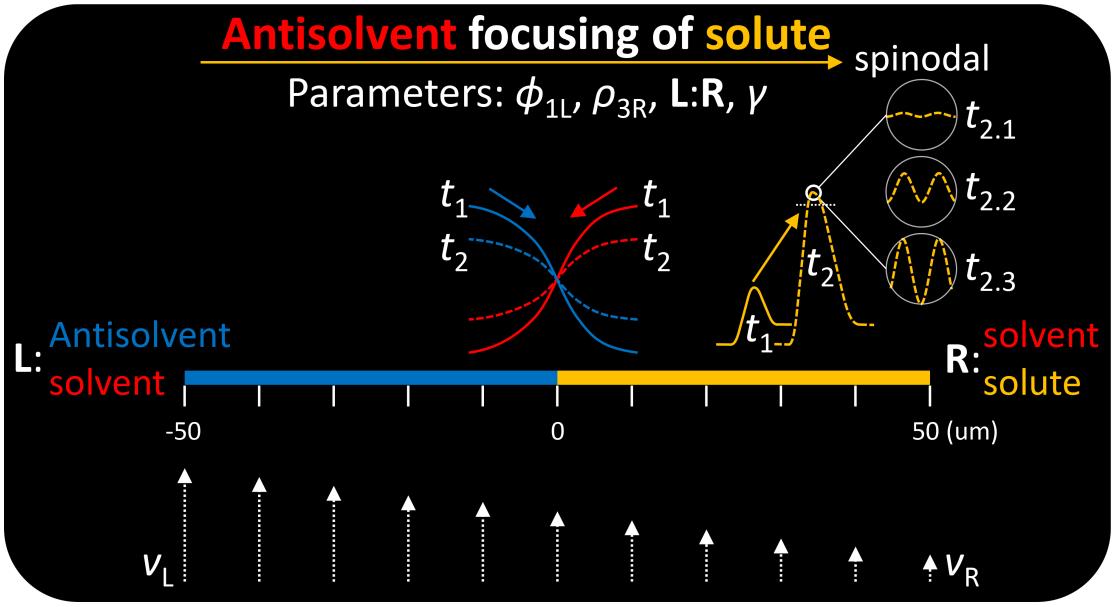

Figure 2. The hypothetical micrometric diffusion couple. The diffusion is limited to one-dimensional across 100 μm. A linear vertical convection velocity field v can be overlayed to simulate agitation, with v_L and v_R being the limiting velocities. At time zero, t_0, two solutions—**L**, a homogeneous mixture of water (1) and 1,4-dioxane (2), and **R**, DBDCS (3) dissolved in 1,4-dioxane (2)—make contact. From t_0, water (1) diffuses into **R**, and 1,4-dioxane (2) into **L**, both toward homogeneity. The influx of the antisolvent raises the energy of the solute, leading to solute uphill diffusion and phase transitions. High enough supersaturation can trigger spinodal decomposition through amplification of composition fluctuations. Control parameters include the initial volume fraction of the water (1) in **L**, ϕ_{1L}, the initial concentration of the DBDCS (3) in **R**, ρ_{3R}, the antisolvent-to-solution size ratio, **L**/**R**, and the agitation shear rate, $\gamma = (v_R - v_L)/(\mathbf{L} + \mathbf{R})$.

A schematic depiction of the evolutions of the concentrations is inset in **Figure 2**. From t_0, water (1) diffuses into **R**, and 1,4-dioxane (2) toward **L**, both toward homogeneity. The influx of the antisolvent raises the energy of the solute, leading to solute uphill diffusion and phase transitions. Our simulations consider solely molecular migration not nucleation[58, 1] or phase interface dynamics[59, 60, 61, 62]. Consequently, our simulation either comes back to homogeneity after the diminishing of the antisolvent gradient or ends up with spinodal decomposition but without the evolution (merging and migration) of particle interfaces.

Chemical potentials of each component of water (1)-[1,4-dioxane] (2)-DBDCS (3) at T_{r} were assessed as a function of composition in Part I[2]. The equations and parameters are given again in Section S1 of the Supporting Information. Essential properties of the three components required for the simulation are listed in Section S2. The density of the water (1)-[1,4-dioxane] (2) system is attached in Section S3, dynamic viscosity in Section S4, thermodynamic factor in Section S5, and mutual Fick diffusion coefficient in Section S6. The self-diffusion coefficient of DBDCS (3) at infinite dilution in water (1)-[1,4-dioxane] (2), estimated using eq. 7, is shown in Section S7. The three pairs of the M-S diffusivities in the ternary mixture were assessed using eq. 5, neglecting the solute's contribution to the viscosity of the mixture. The above comprises the experimental data input for the computations.

Time-dependent simulations of the composition evolutions were conducted with a home-modified *COMSOL* model. The governing equations of the classical field theory are given in Section S8. To explore the impacts of the mixing parameters, the simulation control parameters were swept individually, $\phi_{1\mathrm{L}}$ from 0 to 100 %, $\rho_{3\mathrm{R}}$ from 1-4E to 100 g/L, **L/R** from 1/9 to 30/1 while keeping the total diffusion distance of 100 μm, and γ from -8/s to 8/s while keeping an average vertical velocity of 1 mm/s (Reynolds number $Re = \sim 0.06$ and Péclet number $Pe = \sim 3000$).

4. Antisolvent-induced spinodal decomposition

4.1. Microfluidic fluorescence observation of antisolvent focusing

Figure 3a is the microfluidic observation of antisolvent-induced oiling-out of DBDCS (3) in water (1)-[1,4-dioxane] (2). Two coaxially aligned cylindrical capillaries create a co-flow, where DBDCS dissolved in 1,4-dioxane (2) forms a central jet injected into a peripheral flow of a mixture of water (1)-[1,4-dioxane] (2). After the injection nozzle, the central jet expands due to a mismatch of the co-flow's hydrodynamic velocities, cf. Section S9. The interface between central and peripheral flows vanishes as the refractive indices homogenize with the cosolvent interdiffusion. Instead of crystals, monodispersed (diameter 7.5 ± 0.9 μm) liquid

droplets, interspersed with nanoparticles, periodically emerge 300 μm downstream of the nozzle, corresponding to a precipitation time, $t^* = \sim 0.3$ s. **Figure 3b** displays the fluorescence intensity of DBDCS (3) using a red-yellow color scale. Initially confined within the central capillary, the flux of DBDCS expands with the central jet, but then gradually refocuses into a thin line, with the droplets appear as continuous due to the acquisition time of the fluorescence image. This observation is oiling-out induced by antisolvent focusing (in contrast to hydrodynamic focusing) of the solute.

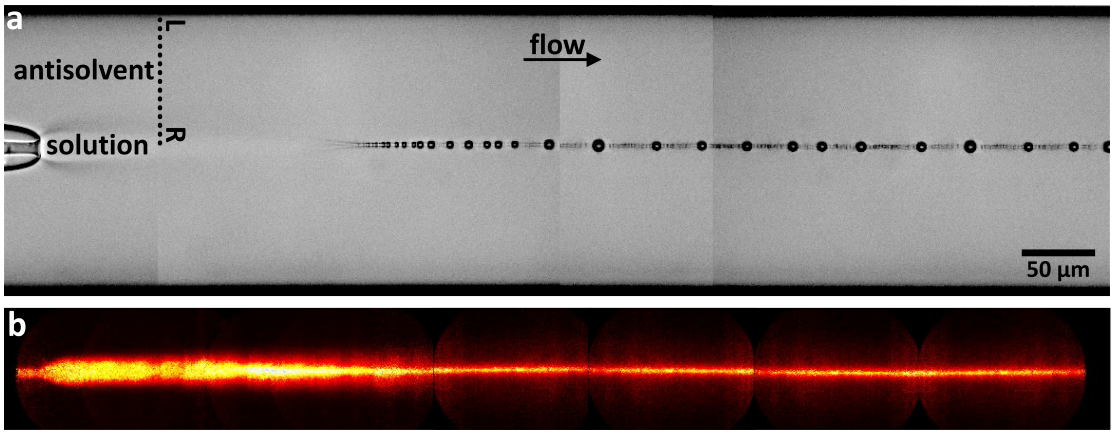

Figure 3. Microfluidic observation of antisolvent focusing and the induced oiling-out of DBDCS (3) in water (1)-[1,4-dioxane] (2). In a coaxial cylindrical system, DBDCS (3) dissolved in 1,4-dioxane (2) forms the central flow, injected in to a peripheral flow of water (1) mitigated with 1,4-dioxane (2). The transmission image (**a**) shows the antisolvent-solvent interdiffusion, indicated by the vanishing flow interface, is followed by the formation of monodispersed droplets. The fluorescence intensity image (**b**) reveals that DBDCS focuses toward the flow center. The dotted line correlates to the diffusion couple, neglecting the Poiseuille velocity profile of the laminar flow. Microfluidic parameters: solute concentration in the central flow, $\rho_{3c} = 5\,\mathrm{g/L}$, antisolvent volume fraction in the peripheral flow, $\phi_{1p} = 50\%$, central flow rate, $Q_c = 30\,\mathrm{nL/min}$, peripheral flow rate, $Q_p = 1\,\mu\mathrm{L/min}$, velocity along flow center, $v_R = 1.1\,\mathrm{mm/s}$, and precipitation time, $t^* = 0.3\mathrm{s}$.

4.2. Antisolvent-induced spinodal decomposition

The dotted line in **Figure 3a** corelates to the hypothetical diffusion couple, disregarding the velocity profile (cf. Section S9) of laminar flow and diffusion in the second dimension. Coupling diffusion and hydrodynamic simulations is useful to predict concentration and supersaturation maps for real applications, as exampled in Section S10. However, this approach falls outside the scope of this paper. We objective is to individually investigate the impacts of each control parameter and elucidate principles general for the mixing in antisolvent crystallization.

Figure 4 showcases two representative simulations illustrating the antisolvent focusing effect: (**a**) solute uphill diffusion followed by downhill diffusion (cf. Video 1), and (**b**) solute uphill diffusion leading to spinodal decomposition (cf. Video 2). The cosolvent composition profiles decay toward homogeneity, cf. Section S9. We are concerned with the behavior of the solute. The mass concentration profiles of DBDCS (3), ρ_3, at exponentially increasing diffusion times, are plotted against the spatial coordinate. The two simulations commence with different solute concentrations, $\rho_{3\mathrm{R}} = 8.8\ \mathrm{g/L}$ in (**a**) and 9 g/L in (**b**), under the same $\phi_{1\mathrm{L}} = 80\%$ and **L/R**=1/1. In both simulations, a wave of DBDCS (3) emerges, depleting on the left while the right remains unchanged. The solute concentration wave progresses toward the good solvent (right side) from 0 to 5 s. It has moved 3 μm within $t = 0.01$ s, then slowing to reach 30 μm by $t = 1$ s. After $t = 0.5$ s, the solute start to accumulate at the right end of the diffusion couple. In (**a**), the solute wave reaches a maximum of 33 g/L, which marks the strength of the antisolvent focusing. It then gradually decays to homogeneity from 5 to 30 s. In (**b**), it reaches a maximum of 35 g/L and triggers a rapid spinodal decomposition from 5 to 6 s trough amplification of concentration fluctuations, resulting in droplets of pure liquid solute (1250 g/L). These nanodroplets can be correlated with amorphous precursors for nucleation. Due to the solute energy raised by the antisolvent (up to $43\mathrm{kJ/mol} \approx 17RT_\mathrm{r}$ upon DBDCS meets water), formation of amorphous clusters upon antisolvent addition is much easier compared with that in a homogeneous solution.

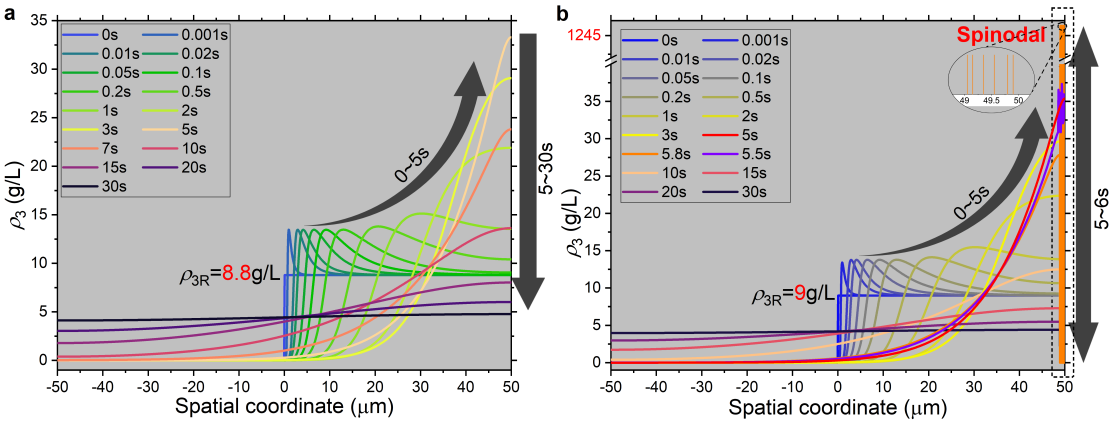

Figure 4. Time-dependent simulations demonstrates two typical scenarios of antisolvent focusing of solute: (**a**) solute uphill diffusion followed by downhill diffusion; (**b**) solute uphill diffusion leading to spinodal decomposition. Mass concentration profiles of the solute, ρ_3, at exponentially growing diffusion times, are plotted against the spatial coordinate, z. Simulation parameters: initial solute concentration in **R**, $\rho_{3\mathrm{R}} = 8.8\,\mathrm{g/L}$ in (**a**) and $9\,\mathrm{g/L}$ in (**b**), with the same initial antisolvent volume fraction in **L**, $\phi_{1\mathrm{L}} = 80\%$, antisolvent-to-solution size ratio, **L**/**R**=1/1, no convection. Components: water (1)-[1,4-dioxane] (2)-DBDCS (3).

Figure 5 illustrates an energy wave generated upon the influx of the antisolvent, where the solute gains energy but equilibrates slower ($D_3^*/D_{12} = \sim 100$, cf. Sections S6 and S7) than the antisolvent. This energy wave advances toward the right end of the diffusion couple with the antisolvent. The solute migration is driven by the slopes of the energy wave, as indicated by the arrows. Diffusion velocity is proportional to the force, and flux is the product of velocity and concentration. The concentration, and thus the flux, is orders of magnitude smaller on the left of the energy wave than on the right, as indicated by the size of the arrows. By the time the energy wave reaches the end of the diffusion couple, although cosolvent mixing is yet halfway complete, the antisolvent gradient can no longer retain the solute, which marks the maximum of the solute concentration being reached simultaneously at the end of **R**. This is when the gradient of the entropic term overcomes the enthalpic term. Afterward, the energy gradient reverses, steering the solute toward homogeneity with kinetics close to exponential decay (due to the diminishing gradient). This is the thermodynamics underlying **Figure 4a**.

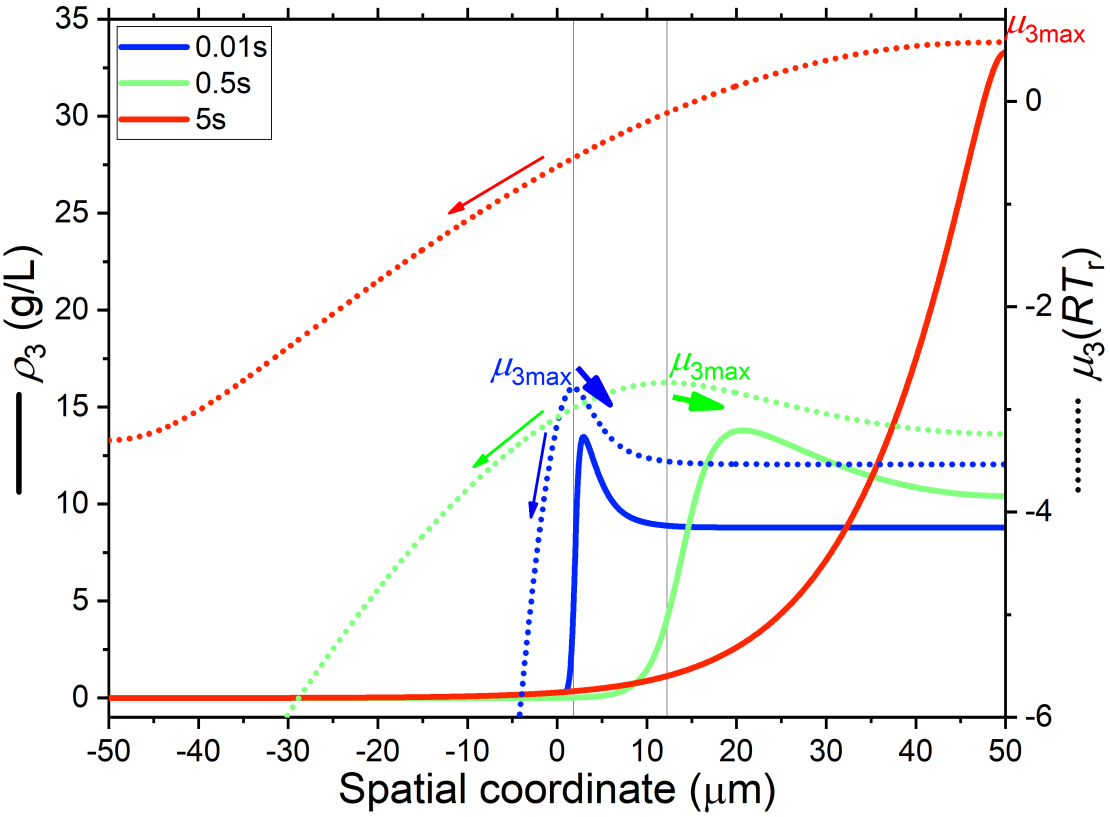

Figure 5. Evolution of solute chemical potential, μ_3, in relations to its concentration, ρ_3. The wave of μ_3 is behind that of ρ_3. The solute migration is driven by the slopes of μ_3, as indicated by the arrows, whose sizes reflect the magnitude of the fluxes. The values of μ_3 is taken relative to the liquid reference state. Simulation parameters: initial solute concentration in **R**, $\rho_{3R} = 8.8\,\mathrm{g/L}$, initial antisolvent volume fraction in **L**, $\phi_{1L} = 80\%$, antisolvent-to-solution size ratio, **L**/**R**=1/1, no convection. Components: water (1)-[1,4-dioxane] (2)-DBDCS (3).

Our simulations do not consider nucleation events. Nevertheless, **Figure 4b** shows continued solute uphill diffusion after 5 s, leading to phase separation. This occurs as the local composition at the wave peak enters the spinodal decomposition region, where an infinitesimal composition fluctuation can amplify spontaneously along the concave directions of the *G*-*x* (Gibbs energy, *G*, as a function of amount fraction composition, *x*, cf. Section S12) function by reducing the energy of the system (cf. Section S13). This is the thermodynamic rationale for **Figure 4b**.

4.3. Two sites for spinodal decomposition

Figure 6 reveals two sites of occurrence for antisolvent-induced spinodal decomposition. The solute concentration profiles of the initial 0.1 s of the spinodal decomposition are shown. In (**a**), with the initial solute concentration $\rho_{3R} = 10\text{g/L}$, the spinodal limit is reached at the wave top by the end of the diffusion couple. With $\rho_{3R} = 20$ g/L, (**b**) demonstrates an amplification of composition fluctuations between the wave waist and top. In (**c**), with $\rho_{3R} = 50\text{g/L}$, separation initiates at the wave waist, while the peak remains stable. With $\rho_{3R} = 100\text{g/L}$, (**d**) predicts spinodal decomposition at the wave waist while the solute concentration wave is still moving toward **R**. Higher initial solute concentrations lead to earlier (from 4.6 s to 1.6 s in (**a-d**)) spinodal decomposition at wave waist. Section S14 gives a mathematical demonstration that antisolvent-induced spinodal decomposition initiates at either the concentration wave top or waist.

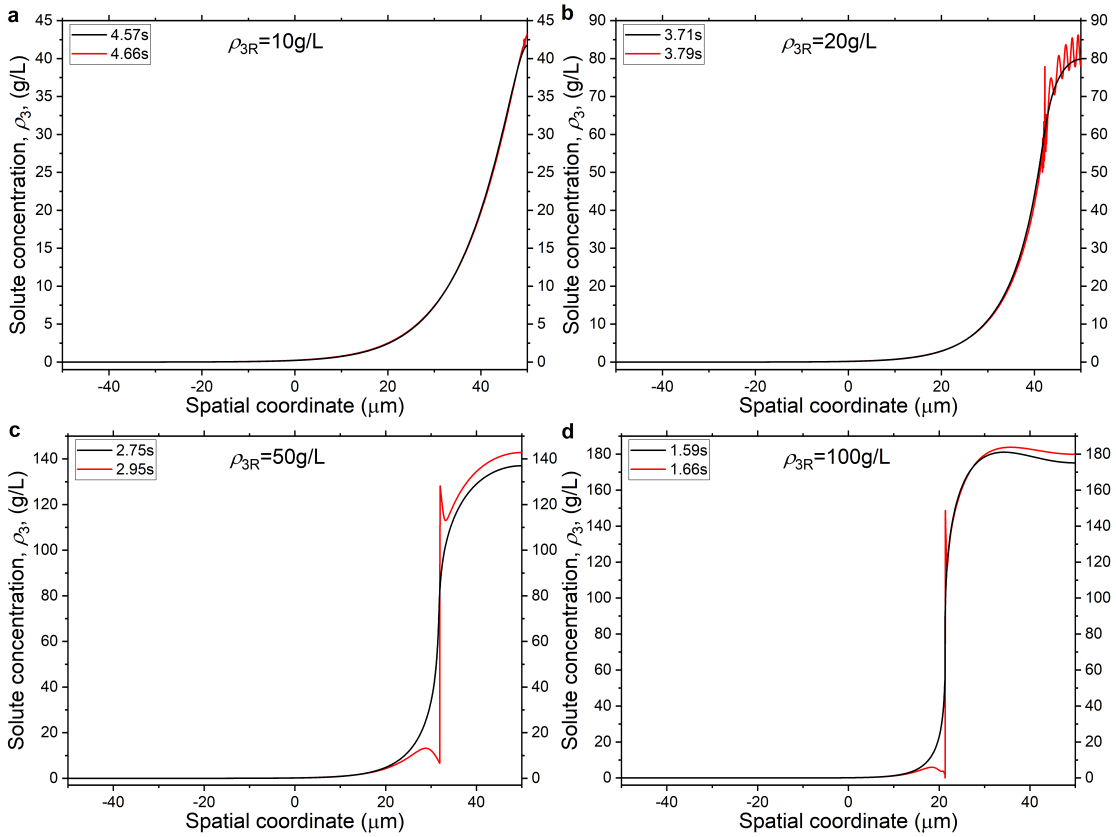

Figure 6. Time-dependent simulations reveal two sites for antisolvent-induced spinodal decomposition: (**a**) at the wave top, (**b**) between the wave waist and top, (**c**) at the wave waist

while the peak is stable, and (**d**) at the waist before the peak reaches the end of the diffusion couple. Concentration profiles of the solute (3), ρ_3, of the initial 0.1 s of spinodal decomposition are plotted against the spatial coordinate. Simulation parameters: initial solute concentration in **R**, $\rho_{3\mathrm{R}} = 10$, 20, 50, and 100 g/L in (**a-d**), respectively, with the same initial antisolvent volume fraction in **L**, $\phi_{1\mathrm{L}} = 80\%$, antisolvent-to-solution size ratio, **L/R**=1/1, no convection. Components: water (1)-[1,4-dioxane] (2)-DBDCS (3).

Figure 7 presents microfluidic observations of the two sites for antisolvent-induced oiling-out. In **Figure 7a** (with a lower solute concentration in the central flow, $\rho_{3\mathrm{c}} = 5\mathrm{g/L}$), oiling-out starts at the flow center and then develops into big droplets. In contrast, **Figure 7b** ($\rho_{3\mathrm{c}} = 8\mathrm{g/L}$) shows nano-droplets forming at the edge of the central jet and then merging (attributed[63] to the Marangoni effect) toward the center. These observations correlate with the simulations in **Figure 6**. The simulations in this paper are in one dimension and without the hydrodynamics (cf. Section S9). We seek to demonstrate the principles, not to reproduce the exact experimental conditions.

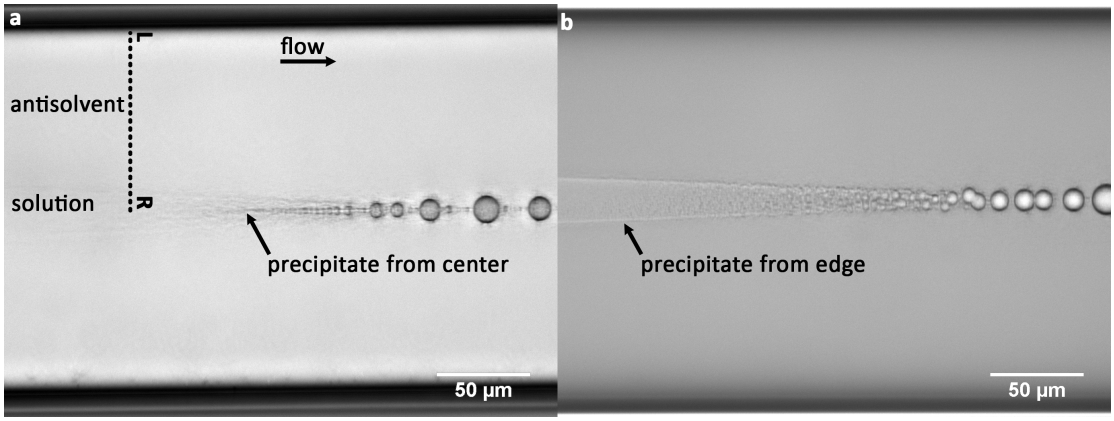

Figure 7. Microfluidic observation of two sites of occurrence for antisolvent-induced oiling-out of DBDCS (3) in water (1)-[1,4-dioxane] (2): (**a**) at the flow center with a lower initial solute concentration, $\rho_{3\mathrm{c}} = 5\,\mathrm{g/L}$, and (**b**) from the edge of the central flow with a higher $\rho_{3\mathrm{c}} = 8\,\mathrm{g/L}$, both under the same antisolvent volume fraction in peripheral flow, $\phi_{1\mathrm{p}} = 80\%$, central flow rate, $Q_{\mathrm{c}} = 370\,\mathrm{nL/min}$, and peripheral flow rate, $Q_{\mathrm{p}} = 1\,\mu\mathrm{L/min}$. The

dotted line correlates to the diffusion couple, neglecting the Poiseuille velocity profile of the laminar flow.

5. Diffusion trajectories on phase diagram

Plotting the evolution of local compositions (diffusion trajectories) on the phase diagram unveils the thermodynamic conditions prior to phase transitions. The phase diagram of water (1)-[1,4-dioxane] (2)-DBDCS (3), calculated in Part I[2], consists regions of dissolution, crystallization, LLPS, and spinodal decomposition, partitioned by the polymorph SLE, metastable LLE, and spinodal limit. **Figure 8** features an example where diffusion trajectories are taken every 5 μm along the diffusion couple. This simulation shows contrasting journeys of local compositions. All voxels in **R** experience an initial increase of ρ_3 (80% increase to 0.18 g/L over 1 s). This corresponds to the overshoot in the solute concentration profile in **Figure 4a** and **Figure 5**. Near the **L-R** interface, the rise of ρ_3 is transient, followed by rapid depletion of the solute (4 orders of magnitude over 0.2 s) as the concentration wave advances toward the end of **R**. Interestingly, the solute depletions at 1 to 20 μm form a curve parallel to the solubilities, which are contours of solute chemical potential[2]. In contrast, near the right end (z between 40 and 50 μm), solute accumulates to a maximum concentration, $\rho_{3\max} = 0.44\text{g/L}$, at $t = 2.5\,\text{s}$, which marks the strength of antisolvent focusing $\rho_{3\max}/\rho_{3\text{R}} = 440\%$. In comparison to **Figure 5** where the antisolvent mitigation fraction $\phi_{1\text{L}} = 80\%$, pure water (1) in contact with the solution reduces the peak time of antisolvent focusing from 5 s to 2.5 s. It reaches the γ-SLE, the β-SLE, and the metastable LLE at 2.8 s, 3.5 s, and 6.4 s, respectively. Since our simulations do not consider nucleation, the diffusion trajectories continue to evolve after entering the metastable regions, which can be justified due to slow kinetics of nucleation. This is followed by show downhill diffusion coming back to the LLE at 18.6 s, with the trajectories for $z < 40\mu\text{m}$ gradually rising toward homogeneity from 2.5 to 30 s.

This simulation demonstrates that even with initial and fully mixed compositions carefully selected below the metastable LLE, local diffusion trajectories can nevertheless enter

the LLPS region (LLE/γ-SLE concentration ratio, $S_{\%} = \sim 5000\%$) upon antisolvent addition and stay there for a prolonged period, which facilitates nucleation of metastable phases. The s-shaped ("serpentine"[8]) characteristics of the diffusion trajectories have been reported by Krishna on the ouzo effect in liquid mixtures. These typical diffusion trajectories, sampled at points equally spaced along the diffusion couple, can be generalized to various antisolvent crystallization scenarios, such as two layers of liquids, two droplets in contact, co-flows, droplets dispersed in a continuous phase, and so on.

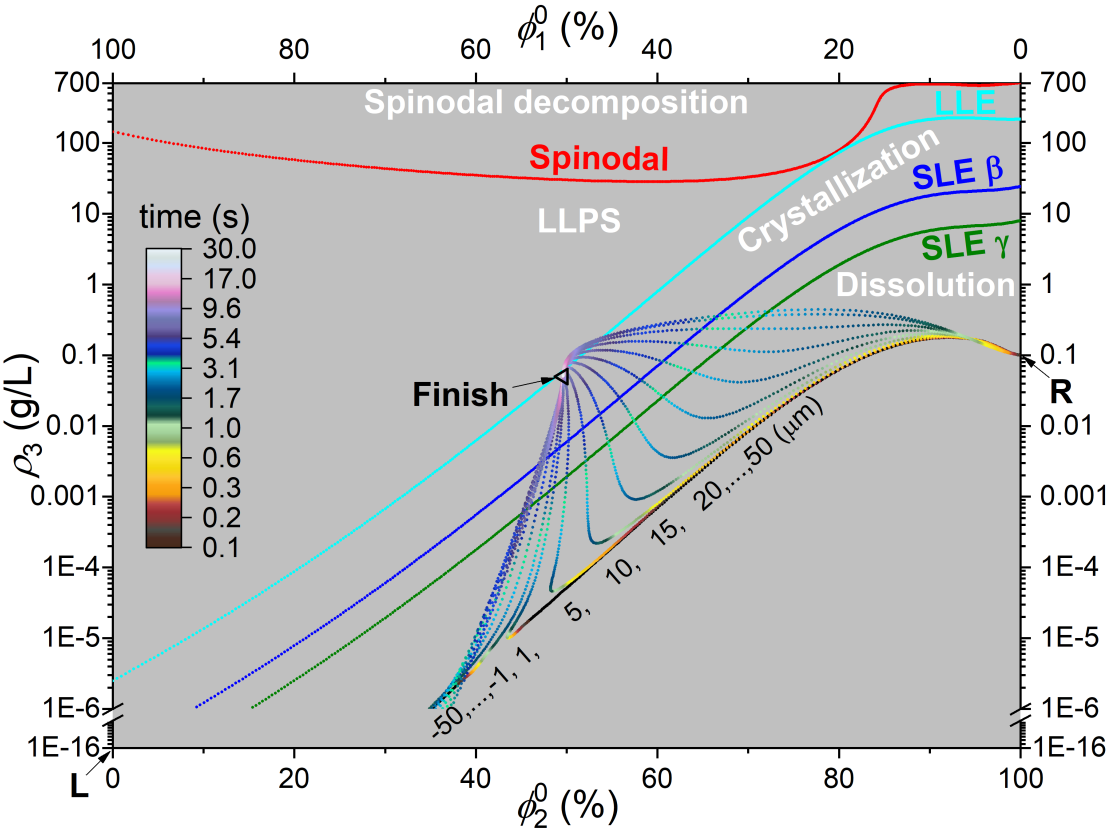

Figure 8. Computational diffusion trajectories of local compositions sampled every 5 μm along the diffusion couple, plotted on the phase diagram of water (1)-[1,4-dioxane] (2)-DBDCS (3) in terms of solute mass concentration, ρ_3, and solute-free solvent volume fractions, ϕ_2^0 and ϕ_1^0. Diffusion time is represented by the color code. The initial compositions are labeled **L** and **R**, and the final composition marked by the triangle. The computational phase diagram[2] consists of the regions of dissolution, crystallization, LLPS, and spinodal decomposition, partitioned by the curves of polymorph SLE, metastable LLE,

and spinodal limit. Simulation parameters: $\rho_{3\mathrm{R}} = 0.1\,\mathrm{g/L}$, $\phi_{1\mathrm{L}} = 100\%$, **L**/**R**=1/1, no convection.

6. Impacts of mixing parameters

6.1. Impact of antisolvent mitigation by good solvent

To simplify the impacts of mixing parameters, we sample diffusion trajectories at ±50μm, the two ends of the diffusion couple. In **Figure 9a**, the initial antisolvent fraction in **L**, $\phi_{1\mathrm{L}}$, was swept from 0 to 100 % while maintaining $\rho_{3\mathrm{R}} = 7.2\,\mathrm{g/L}$ (corresponding to a ρ_3/γ-solubility saturation ratio $S_{\%} = 80\%$), **L**/**R**=1/1, and no convection. For $\phi_{1\mathrm{L}} = 0\%$, the solute concentration profile decays toward homogeneity, cf. Section S15. As $\phi_{1\mathrm{L}}$ increases, diffusion trajectories enter different phase regions. With $\phi_{1\mathrm{L}} = 30\%$ and $\phi_{1\mathrm{L}} = 40\%$, the diffusion trajectories stay between the γ and β-SLE the whole time. To produced crystals of the γ phase, these are good conditions. The diffusion trajectories of $\phi_{1\mathrm{L}} = 50\%$ and $\phi_{1\mathrm{L}} = 60\%$ cross the β-SLE at 4.8 s and 3.2 s, respectively, and then stay below the metastable LLE, predicting favorable conditions for producing the β polymorph. For $\phi_{1\mathrm{L}} > 65\%$, diffusion trajectories enter the LLPS region, specifically, $\phi_{1\mathrm{L}} = 90\%$ at 6.3 s and $\phi_{1\mathrm{L}} = 100\%$ at 2.8 s. These are conditions that can induced LLPS. The diffusion in $\phi_{1\mathrm{L}} = 90\%$ and 100% end up with wave-top spinodal decomposition upon encountering the spinodal curve at 4.0 s and 3.0 s, respectively. Whereas, LLPS of $65\% < \phi_{1\mathrm{L}} \leq 87\%$ need to go through nucleation.

The strength of the antisolvent focusing of the solute is dominated by the antisolvent gradient. An increased antisolvent fraction in contact with the solution enhances solute uphill diffusion during a longer time. With $\phi_{1\mathrm{L}}$ increasing from 10 to 87%, $\rho_{3\mathrm{max}}/\rho_{3\mathrm{R}}$ increases from 106% ($\rho_{3\mathrm{max}} = 7.6\mathrm{g/L}$, supersaturation ratio $S_{\%} = 104\%$) to 430% ($\rho_{3\mathrm{max}} = 31\mathrm{g/L}$, $S_{\%} = \sim 7000\%$), and the corresponding time from 0.6 s to 4.2 s. $S_{\%}$ continues to increase after the $\rho_{3\mathrm{maxi}}$, as the solubilities decrease exponentially with the increase of the fraction of the antisolvent. The maximum supersaturation, $S_{\%\mathrm{max}}$, occurs when the slope of the diffusion trajectory is parallel to the solubility curve. The greatest $S_{\%\mathrm{max}} = \sim 70000\%$ ($\rho_3 = 45\mathrm{g/L}$) is

reached by the diffusion trajectory of $\phi_{1\mathrm{L}} = 87\%$ at 11 s. Higher supersaturations could be achieved by the diffusion trajectories of $\phi_{1\mathrm{L}} = 90\%$ and 100%, but they terminate in spinodal decomposition.

Figure 9a demonstrates how adjusting the fraction of the antisolvent mitigated by the good solvent can effectively orient the crystallization toward different polymorphs. This approach allows for the fully mixed composition to be designed into metastable phase regions but also diffusion trajectories to stay above the designed concentrations for prolonged periods. Elevated supersaturations and extended diffusion times offer favorable conditions for the nucleation of metastable phases. Pure antisolvent rapidly induces oiling-out through spinodal decomposition without nucleation.

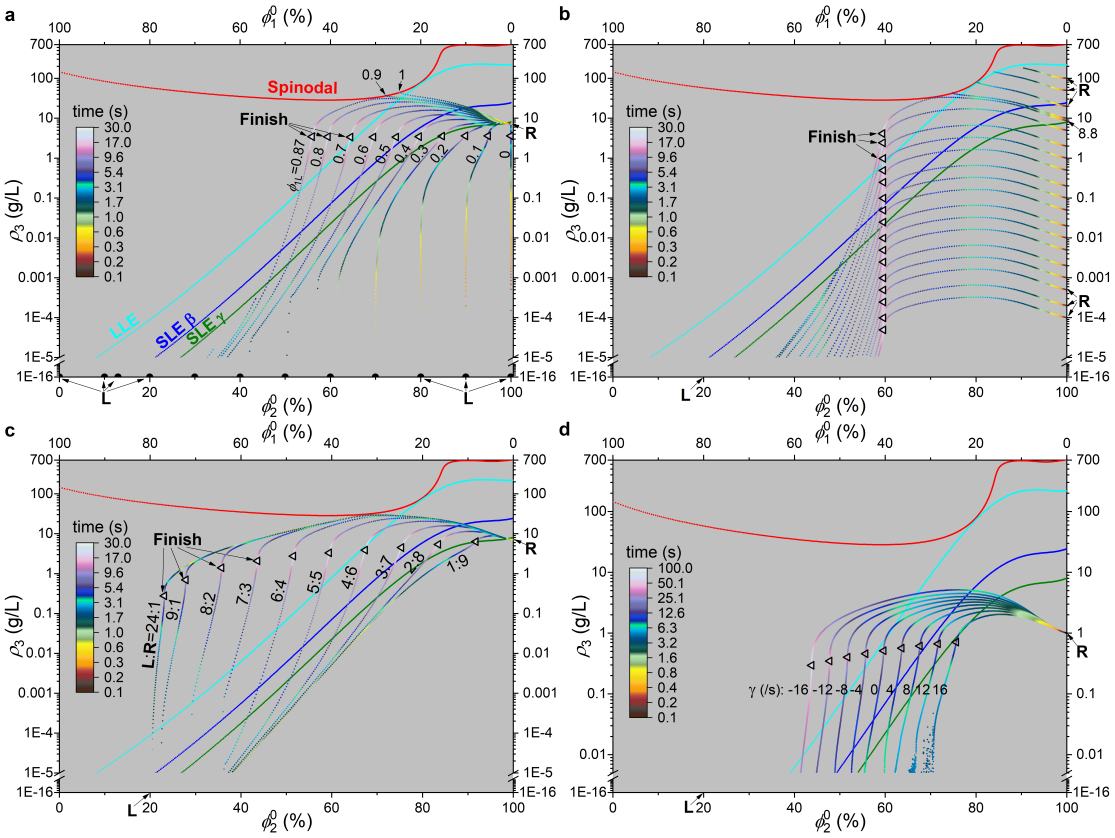

Figure 9. Impacts of control parameters on antisolvent mixing in water (1)-[1,4-dioxane] (2)-DBDCS (3). Control parameters are examined individually: (**a**) initial antisolvent fraction in **L**, $\phi_{1\mathrm{L}}$, (**b**) initial solute concentration in **R**, $\rho_{3\mathrm{R}}$, (**c**) antisolvent-to-solution size ratio, **L/R**, and (**d**) agitation shear rate, γ. Diffusion trajectories are sampled at two ends of the diffusion

couple. The color code represents the diffusion time. They are overlayed on the phase diagram, in terms of solute mass concentration, ρ_3, and solute-free solvent volume fractions, ϕ_2^0 and ϕ_1^0. The curves of polymorph SLE, metastable LLE, and spinodal limit are based on thermodynamic calculation[2]. Simulation conditions: (**a**) $\phi_{1\mathrm{L}}$ as labeled, $\rho_{3\mathrm{R}} = 7.2\ \mathrm{g/L}$, **L/R**=1/1, no agitation; (**b**) $\rho_{3\mathrm{R}}$ reads on the right axis, $\phi_{1\mathrm{L}} = 80\%$, **L/R**=1/1, no agitation; (**c**) **L/R** as labeled, $\rho_{3\mathrm{R}} = 7\ \mathrm{g/L}$, $\phi_{1\mathrm{L}} = 80\%$, no agitation; and (**d**) γ as labeled, average convection velocity 1 mm/s, $\rho_{3\mathrm{R}} = 1\ \mathrm{g/L}$, $\phi_{1\mathrm{L}} = 80\%$, **L/R**=1/1. The initial compositions are labeled **L** and **R**, and the stationary state compositions marked as triangles.

6.2. Impact of solute concentration

Figure 9b sweeps the initial solute concentration in **R**, $\rho_{3\mathrm{R}}$, from 1E-4 to 100 g/L, read from the right axis, while holding $\phi_{1\mathrm{L}} = 80\%$, **L/R**=1/1, and no convection. Under constant $\phi_{1\mathrm{L}}$, diffusion trajectories demonstrate clear parallelism, offset by $\rho_{3\mathrm{R}}$. A $\rho_{3\mathrm{max}}/\rho_{3\mathrm{R}} = \sim 330\%$ at ~3.1 s marks the strength of the antisolvent focusing. **Figure 10a** confirms the parallelism of the concentration kinetics, with ρ_3 in all simulations reach the maximum simultaneously. An exception occurs at $\rho_{3\mathrm{R}} = 8.8\mathrm{g/L}$, which exhibits "stickiness" toward the spinodal limit (**Figure 9b**) and slower kinetics (**Figure 10a**). This is because diffusion driving forces diminish near the spinodal limit, cf. Section S13, which makes the solute migration stagnant on the plateau (**Figure 10a**) between *t*=3.1 to 4.9 s. Above that, **Figure 9b** shows that the diffusion trajectories of $\rho_{3\mathrm{R}} = 10\mathrm{g/L}$ and $20\mathrm{g/L}$ terminate at the spinodal limit at 4.7 s and 3.7 s, respectively, due to wave-top spinodal decomposition, as in **Figure 6a**. Whereas the diffusion trajectories of $\rho_{3\mathrm{R}} = 50\mathrm{g/L}$ and $100\mathrm{g/L}$ terminate before reaching the spinodal curve at 3.0 s and 1.7 s, due to wave-waist spinodal decomposition, as in **Figure 6c** and **Figure 6d**.

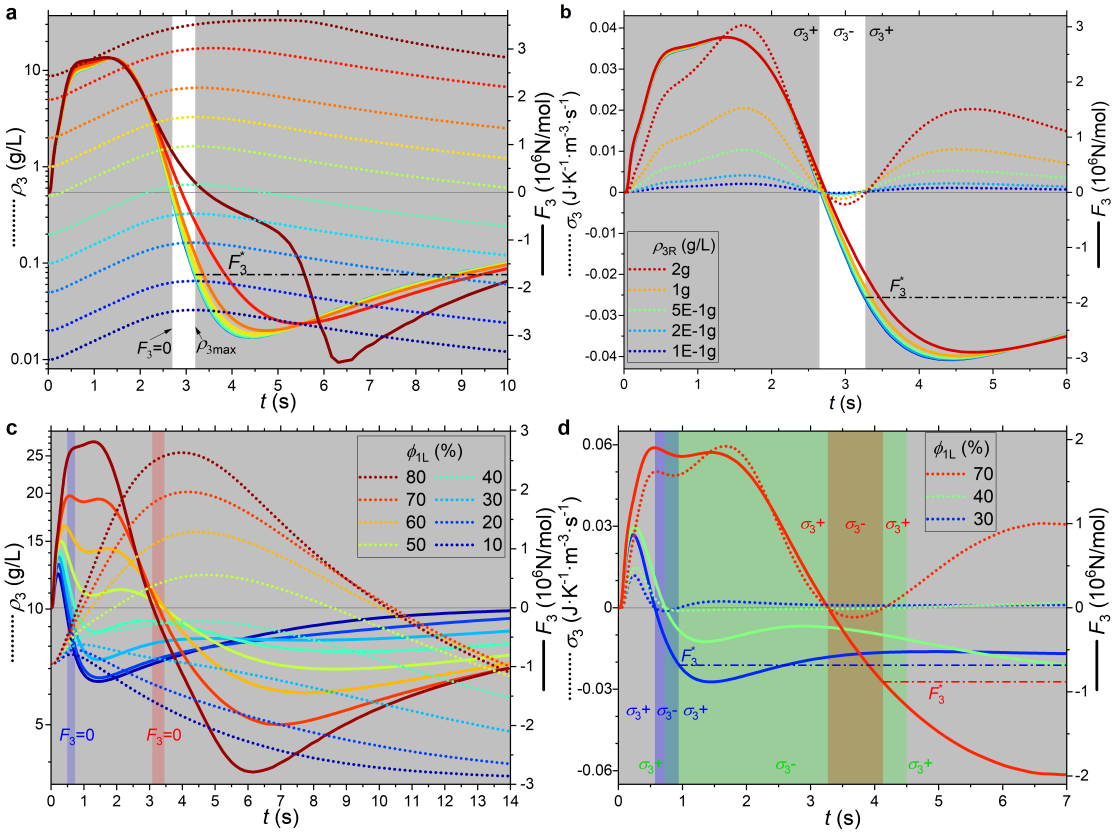

Figure 10. Evolution of the entropy production rate, σ_3, the driving force, F_3, and the concentration, ρ_3, of the solute (3) in **R** at 49 μm: (**a**, **b**) impact of initial concentration in **R,** ρ_{3R}; (**c**, **d**) impact of initial antisolvent volume fraction in **L**, ϕ_{1L}. The maximum solute concentration, ρ_{3max}, lags behind the direction-change-time of F_3, with σ_3 being negative between these two events. F_3 is dominated by ϕ_{1L}, and thus the kinetics. These are the same simulations of **Figure 9a** and **Figure 9b.** Simulation conditions: no convection, (**a**, **b**) $\phi_{1L} =$ 80%, **L**/**R**=1/1; (**c**, **d**) $\rho_{3R} = 7.2\ \mathrm{g/L}$, **L**/**R**=1/1. Components: water (1)-[1,4-dioxane] (2)-DBDCS (3).

The parallelism in the trajectories when varying the initial solute concentration result from the thermodynamic behavior of poorly soluble solutes in cosolvents. The chemical potential of the solute at dilute concentrations demonstrate a log-linear dependence on the solvent composition, with the solute concentration been an offset.[2] Since the solute is a trace component, the multicomponent diffusion is dominated by the solvents. The cosolvent composition map evolves independently of solute concentration. Solute molecules move under

this energy field, whose gradient (the force field and thus the velocity field) is irrelevant to the initial solute concentration (the offset term in the energy). Hence, the rate of change is directly proportional to the local solute concentration. This makes the shape and kinetics of diffusion trajectories independent of initial concentration. The concentration map of the solute will be translated as the initial concentration varies. A mathematical demonstration is attached in Section S16.

6.3. Entropy production and force

Figure 10a and **Figure 10b** presents the driving force for solute migration, F_3, and the associated entropy production, σ_3, with varied $\rho_{3\mathrm{R}}$ from the simulations **Figure 9b**. They are sampled at $z = 49\mathrm{um}$ to not be zero. Despite ρ_3 varies orders of magnitude, F_3 remain unchanged except when near the spinodal decomposition limit. As a trace component, multiplying the solute concentration map by a constant will not change the force field, cf. eq. S26. Before $\rho_{3\mathrm{max}}$, F_3 is positive, driving the solute to accumulate toward the good solvent volume. Right before $\rho_{3\mathrm{max}}$, F_3 changes direction, but the solute, for a period of ~0.5 s (as indicated by the white background), is moving toward the opposite direction. This movement is the manifestation of the drag on the solute by the solvent and antisolvent, which depends on the fluxes and coefficients. In our simulation, the solute follows the movement of water to the end of **R**. In Section S16, we make an approximation that the diffusion of a trace component can be decoupled from other components. **Figure 10** shows that this approximation does not stand when the driving force is small. After $\rho_{3\mathrm{max}}$, solute starts to follow F_3 and diffuses toward homogeneity. The driving force needed to overturn the solute molecules, F_3^*, is about -1.5 MN/mol. This gives an estimation of the drag force, $-F_3^*$. The driving force is between ±3 MN/mol. Most of time, thermodynamics is dominating the solute diffusion. Only when $F_3 < F_3^*$, the drag with other fluxes is observable. But F_3 is dominated by the antisolvent gradient (cf. eq. S36), so the solute uphill diffusion is determined by the influx of the antisolvent, through thermodynamics, not hydrodynamics. This makes the antisolvent focusing different from the uphill diffusion caused by inter-flux coupling or phase instability.

The transient opposite directions of F_3 and J_3 result in negative entropy production in **Figure 10b**. The time when σ_3 turns back to positive correspond to $\rho_{3\max}$ and F_3^*. This is not against the second law of thermodynamics. A negative entropy production by a trace component is easily annihilated by the positive entropy produced by other fluxes. At this moment, the local entropy production by water (1) is ~8W·m^{-3}·K^{-1}, that of 1,4-dioxane (2) ~1.5W·m^{-3}·K^{-1}, and that of DBDCS (3) ranges (depending on the concentration) from 5E-3 to 1.5E-7 8W·m^{-3}·K^{-1}. The transient local consumption of entropy relies on a much greater total positive entropy production.

In **Figure 10c** and **Figure 10d** displays F_3 and σ_3 with varied $\phi_{1\mathrm{L}}$ from the simulations in **Figure 9a**. **Figure 10c** shows that a larger antisolvent gradient causes a stronger antisolvent focusing during a longer diffusion time. The stronger antisolvent focusing, marked by higher $\rho_{3\max}$, is due to a greater F_3. F_3 is the gradient of the solute chemical potential (cf. eq. 4). The influx of water (1) elevates the energy of DBDCS (3) (up to $43\mathrm{kJ/mol} \approx 17RT_\mathrm{r}$). The solute energy gradient is a projection of the antisolvent gradient. The larger the antisolvent gradient, the larger the solute energy gradient. A lager antisolvent gradient takes longer time to dissipate, therefore, a prolonged focusing effect.

Figure 10c further shows that the kinetics of antisolvent come in two groups: with $\phi_{1\mathrm{L}}$ from 10% to 40%, F_3 changes direction at t=~0.6 s, as indicated in blue background in **Figure 10c**; and with $\phi_{1\mathrm{L}}$ from 50% to 80% at t=~3.3 s, indicated in red background. So are the concentration evolutions, whose maxima are slightly behind the direction-change-time of F_3, as indicated by the negative σ_3 (blue and red background) in **Figure 10d**. An exception is the intermediate $\phi_{1\mathrm{L}} = 40$, whose F_3 is within ±0.5 MN/mol for a long time, as indicated by the green background, resulting in a long period (from t=0.7 s to t =4.5 s) of negative entropy production. F_3^*, the driving forces to overcome the drag is -0.6 MN/mol for $\phi_{1\mathrm{L}} = 30\%$, -0.9 MN/mol for $\phi_{1\mathrm{L}} = 70\%$. A greater antisolvent gradient causes its larger flux, resulting in a larger drag on the solute (cf. eq. 3). Our simulations show that solute uphill diffusion is general

upon antisolvent influx. It is driven by the solute energy wave generated by the antisolvent influx, not a manifestation of inter-flux drags or phase instability.

6.4. Impact of antisolvent-to-solution size ratio

Figure 9c displays the impact of antisolvent-to-solution size ratio, **L/R**, while holding the total diffusion distance to 100 μm, $\rho_{3\mathrm{R}} = 7\,\mathrm{g/L}$, $\phi_{1\mathrm{L}} = 80\%$, and no convection. Increasing the antisolvent-to-solution size ratio not only modifies the fully mixed composition but also the enhances strength of the antisolvent focusing and accelerates the kinetics. **Figure 11a** plots the evolution of solute concentration at the right end of the diffusion couple. As **R** decreases from 80 μm (**L/R**=2:8) to 10 μm (**L/R**=9:1), $\rho_{3\mathrm{max}}$ escalates from 160% ($\rho_3 = 11\mathrm{g/L}$, $S_{\%} = 200\%$) to 420% ($\rho_3 = 29\mathrm{g/L}$, $S_{\%} = 1\mathrm{E}4\%$), with the corresponding times dropping from 5.6 s to 0.2 s. For **L/R**>7:3 (**R**<30 μm), trajectories exhibit "stickiness" toward the spinodal limit (red curve). A highest $S_{\%}$ of 1E7% is achieved with **L/R**=24:1 (**R**=4 μm) at 1.8 s. Further increase of **L/R** can yield higher $S_{\%}$ values within shorter diffusion times. Investigating the impact antisolvent-to-solution size (volume) ratio is useful, given the significant variation in the scale between antisolvent and solution in practical scenarios. Our simulations show that the smaller droplets/layers the solution breaks into, the higher and faster the solute will be focused toward metastable phase transitions.

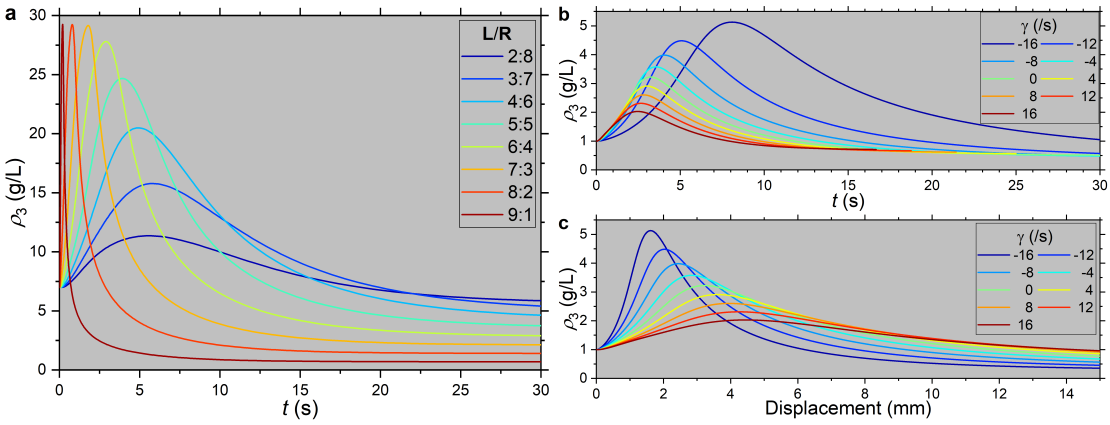

Figure 11. Impacts of (**a**) antisolvent-to-solution size ratio, **L/R**, and (**b** and **c**) agitation shear rate, γ, on the kinetics of solute concentration, ρ_3, sampled at the right end of the diffusion couple. These are the same simulations in **Figure 9c** and **Figure 9d**. The solute concentration

plotted against time in (**b**) and displacement in (**c**). Simulation conditions: (**a**) initial concentration in **R**, $\rho_{3\mathrm{R}} = 7\,\mathrm{g/L}$, initial antisolvent volume fraction in **L**, $\phi_{1\mathrm{L}} = 80\%$, no agitation; and (**b-c**) $\rho_{3\mathrm{R}} = 1\,\mathrm{g/L}$, $\phi_{1\mathrm{L}} = 80\%$, **L**/**R**=1/1, average convection velocity 1 mm/s. Components: water (1)-[1,4-dioxane] (2)-DBDCS (3).

6.5. Characteristic times of oiling-out

In the microfluidic experiment, we noticed that precipitation time is inversely proportional to the central/peripheral flow ratio. In **Figure 12a**, the peripheral flow rate was increased 20 times, from 4 to 80 $\mu\mathrm{L/min}$, whilst the central flow rate was fixed. The flow velocity increased 20 times, from 2 to 39 mm/s. The size of the droplets of the oiling-out decreases with the increase of the peripheral flow rate. However, the precipitation position did not move. This means, by changing the **L**/**R** ratio, the characteristic time of oiling-out decreased 20 times, from 0.22 to 0.01 s. In **Figure 12b**, we plot the times corresponding to $\rho_{3\mathrm{max}}$ from **Figure 9c**. The simulation exhibits same behavior as experimental measurement. The slope of the simulations is 2 times of that of the experiment. This can be adjusted by many parameters, such as the diffusion coefficient, thermodynamic parameters, antisolvent fraction in **L**, convection velocity field (cf. Section S9), simulation in one dimension, polar or spherical coordinate systems, and so on. But our simulations and experiment agree in principle that the characteristic time of oiling-out increases linearly with the square of the length of **R**.

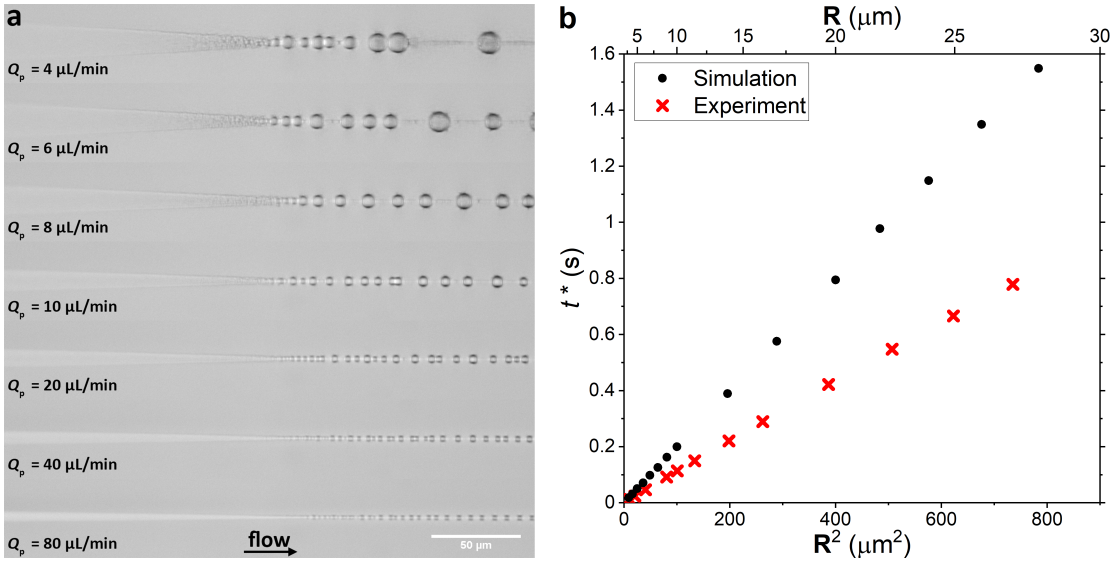

Figure 12. Characteristic time of antisolvent-induced oiling-out as a function of the length of the solution, **R**, in water (1)-[1,4-dioxane] (2)-DBDCS (3). (**a**) Microfluidic observation of a stationary precipitation position, $d^* = 430\mu m$, despite the increase of the flow rate of the antisolvent by 20 times, from 2 to 39 mm/s, which indicates that the characteristic time of oiling-out decreased 20 times, from 0.22 to 0.01 s. (**b**) Diffusion time at the peaks of the diffusion trajectories, t^*, taken from **Figure 9c**, exhibits quadratic dependence on **R**, which agrees with the microfluidic observation. The difference in the slopes can be adjusted by the diffusion coefficient, thermodynamic parameters, antisolvent fraction in **L**, convection velocity field, simulation in one dimension, polar or spherical coordinate systems, and so on. Microfluidic parameters in (**a**): solute concentration in central flow, $\rho_{3c} = 8\,\mathrm{g/L}$, antisolvent volume fraction in peripheral flow, $\phi_{1p} = 30\%$, central flow rate, $Q_c = 148\,\mathrm{nL/min}$, and peripheral flow rate, $Q_p = 4{\sim}80\,\mu\mathrm{L/min}$. Simulation parameters in (**b**) $\rho_{3R} = 7\,\mathrm{g/L}$, $\phi_{1L} = 80\%$, no convection.

6.6. Impact of agitation shear rate

Agitation is a common practice to accelerate the mixing. **Figure 9d** examines the impact of rate of agitation upon antisolvent addition. We control the shear rate in a linear velocity field vertical to the diffusion direction to simulate agitation. A negative shear rate means the antisolvent transfers momentum (moves faster) than the solution, and vice versa. A

change of the shear rate from 0 (the limiting velocities, cf. **Figure 2**, v_L=v_R=1 mm/s) to -16/s (v_L=1.8 mm/s and v_R=0.2 mm/s) results in the strength of antisolvent focusing, $\rho_{3\max}/\rho_{3R}$, increasing from 330% at t=3.1 s to 510% at 8.1 s (cf. **Figure 11b**), yet with the displacement of the voxel at the right end reduced from 3.2 mm to 1.6 mm (cf. **Figure 11c**). The triangles in **Figure 9d**, moving from below the γ-SLE deep into the LLPS region, reflects the composition of a local stationary state not yet compensated by the medium from other dimensions, which depends on a drastic change in the convection velocity field. The change in the displacement is due to the change in the v_R. A faster convection in the antisolvent exposes the solution to more antisolvent during a longer time. Agitation in the solution causes an opposite effect. These simulations show that faster agitation in the antisolvent effectively enhances the focusing effect of the solute for a prolonged diffusion time, resulting in local compositions deep into the LLPS region, and thus oiling-out.

7. Characteristic shape of diffusion trajectories

Our simulations (**Figure 8** and **Figure 9**) confirm the s-shaped (serpentine[8]) diffusion trajectories previously reported by Krishna in his study on the ouzo effect. Now let us examine the thermodynamics behind this characteristic trajectory shape. **Figure 13a** present typical directions of diffusion couples on the phase diagram overlayed with solute chemical potential. The chemical potential will drive the solute to migrate from high energy to low energy. The diffusion couples, **L-H+**, **L-H0**, **L-H1**, **L-H***, and **L-H2** have the same solute gradient but different antisolvent gradient, ranging from positive to negative. In **L-H+**, **L-H0**, **L-H1**, the solute migration is downhill from high concentration to low concentration, indicated by the yellow arrows, as the high concentration happen to also have higher energy. As the gradient of the antisolvent increases, **L-H*** represents the limit of the antisolvent focusing of solute, as it is parallel to the contour of μ_3, and, thus, almost stagnant solute migration. Under a large (negative) antisolvent gradient, such as in **L-H2**, the higher concentration has low energy, so the solute migrates toward higher concentrations. It is the energy gain (up to ~40kJ/mol) of DBDCS (3) upon antisolvent addition that drives this process from chaos to order.

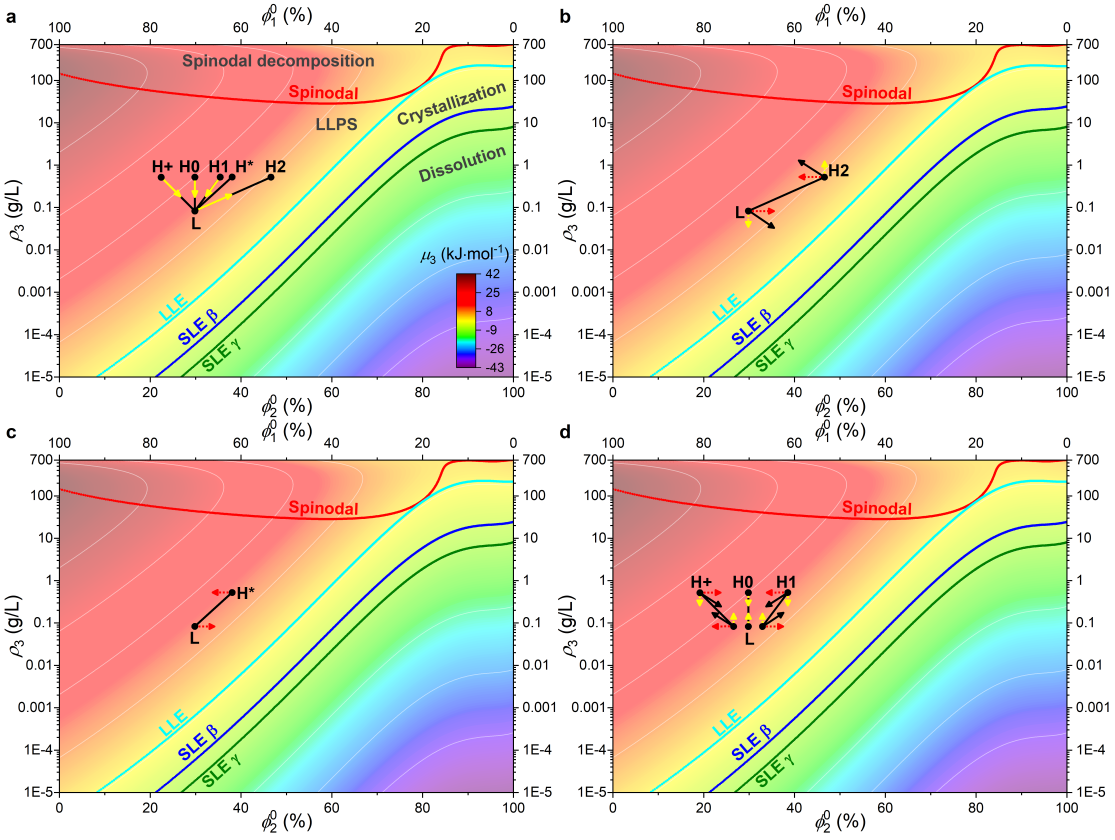

Figure 13. Thermodynamic explanation for the "serpentine" (s-shaped) characteristic shape of the diffusion trajectories in antisolvent crystallization. The chemical potential of the solute (3), μ_3, relative to the liquid reference state, is shown as a color map with white contours, overlaid on the phase diagram of water (1)-[1,4-dioxane] (2)-DBDCS (3), in terms of solute mass concentration, ρ_3, and solute-free solvent volume fractions, ϕ_2^0 and ϕ_1^0. Some representative directions of diffusion couples with the same solute gradient but different antisolvent gradients are presented. (**a**) Direction of solute migration: **L-H2** exhibiting uphill diffusion, **L-H*** (parallel to the contour of μ_3) indicating the limit between uphill and downhill diffusion, and **L-H1**, **L-H0**, **L-H+** representing downhill diffusion under positive, zero, and negative antisolvent gradient, respectively. (**b-d**) Directions of composition evolution. The black arrows indicate the vector (not to scale) of the composition evolution directions, the red and the yellow arrows are the components affiliated with 1,4-dioxane (2) and DBDCS (3), respectively. The fluxes of the solvents are generally much larger than that of the solute. A large antisolvent gradient causes the diffusion trajectories to be s-shaped.

In **Figure 13b-d**, we decompose the vector (not to scale) of the composition evolutions into two independent components for the solute and the good solvent, respectively. The diffusion of the cosolvents is toward homogeneity, cf. Section S11. This is shown by the red arrows. For **L-H2** in **Figure 13b**, the migration of the solute from **L** to **H2** leads to an increase of concentration in **H2** and a decrease of concentration in **L**, shown by the yellow arrows. As a result, the black arrows give the direction of the composition evolution. For **L-H*** in **Figure 13b**, the solute migration is stagnant, therefore, direction of the composition evolution is dominated by the solvent diffusion. For **L-H0** in **Figure 13d**, since the antisolvent gradient is zero, the composition evolution is dominated by the solute toward homogeneity. For **L-H+** and **L-H1** in **Figure 13d**, both the solute and solvents migrations are toward homogeneity, but the fluxes of the solvents are much stronger than that of the solute. Therefore, the direction of evolution in **L-H+** and **L-H1** can slightly deviated from a straight line (despite the logarithmic scale).

Same conclusions can be draw by moving the diffusion couples anywhere under the spinodal decomposition limit. Of course, the simulation has more than two voxels. It consists infinite pairs of infinitesimal sections of the such hypothetical diffusion couples, evolving in ensemble. **Figure 13** shows that s-shaped diffusion trajectories are characteristic for antisolvent crystallization, and that the antisolvent focusing of solute is general in antisolvent crystallization.

Conclusions

With the chemical potentials assessed in Part I[2], moving from equilibrium to irreversible thermodynamics, we investigate molecular migration kinetics prior to antisolvent-induced phase transitions. Time-dependent simulation of a hypothetical diffusion couple has been performed in the frame of the Maxwell-Stefan model with the chemical potential gradients as driving forces. The simplified model captures general scenarios where antisolvent and solution contact on a micrometric scale, such as co-flows, droplets in contact, droplets dispersed in a continuous phase, liquid layers, and so on. The example ternary system is water-[1,4-dioxane]-DBDCS. But the conclusions are not limited to the specific system.

The antisolvent influx significantly raises the chemical potential of the solute (up to ~40kJ/mol), generating an energy wave that drive the solute to focus toward the good solvent. The accumulation of solute can induce spinodal decomposition (**Figure 4**). Microfluidics (**Figure 7**) and simulations (**Figure 6**) revealed two positions of antisolvent-induced spinodal decomposition: wave top vs wave waist on the solute concentration profile.

Our simulations (**Figure 9**) show that the strength of the antisolvent focusing is dominated by the antisolvent gradient. The diffusion driving force, and thus the strength of the focusing effect, increases with the antisolvent gradient. The initial solute concentration acts as an offset on the diffusion trajectories. Faster agitation in the antisolvent effectively enhances the strength of antisolvent focusing, resulting in local compositions deep into the LLPS region, and thus oiling-out. Microfluidics and simulations concur that the characteristic time of oiling-out increase quadratically with diffusion distance in the solution (**Figure 12**). Elevated supersaturations and extended diffusion times offer favorable conditions for the nucleation of metastable phases. Pure antisolvent rapidly induces oiling-out through spinodal decomposition without nucleation. These conclusions are general for process design of antisolvent crystallization: larger antisolvent gradient, faster agitation in the antisolvent, and breaking the solution into smaller droplets/layers all enhances antisolvent focusing effect and thus oiling-out.

By analyzing the rate of entropy production (**Figure 10**), we show that the solute diffusion can largely be decoupled from the cosolvents. However, the solute is migration on a force field dominated by the antisolvent gradient. Only for a transient period when the force is small (<~1 MN/mol), the uphill diffusion is attributed to inter-flux drag. During this transient period, the local entropy production due to solute migration is negative. It relies on a much greater positive entropy production from other fluxes. Finally, by analyzing the vectors of composition evolution in different diffusion couples (**Figure 13**), we conclude that solute uphill diffusion is general upon the influx of antisolvent, but not a manifestation of inter-flux drag or phase instability. It is the solute energy gain upon antisolvent addition that drives this process from chaos to order.

Our Part I and II together bring a unified methodology, from solubility measurement to kinetic simulation, addressing the competition between antisolvent crystallization and oiling-out. The methodology and the insights obtained through this study can be extended to the parameter optimization for other antisolvent crystallization systems. There are new potentials and challenges: simulation of molecular migration coupled with other fields, such as hydrodynamics, laser optical gradient, electric field, centrifugal force, high pressure, high gravity, temperature field, and so on; phase field simulation of crystal growth based on the map of diffusion and hydrodynamics in microfluidics; simulation of antisolvent crystallization coupled with temperature control or under supercritical conditions with temperature or pressure as independent variables. We hope that our work will inspire more studies on the competition between oiling-out and crystallization from both theoretical and experimental standpoints.

Experimental section

Materials

The solute, DBDCS, was synthesized as described in the previous paper[22]. The antisolvent was ultrapure water obtained through a *Milli-Q* filtration system. The organic solvent used was 1,4-dioxane (*CARLO ERBA*, purity ≥ 99.5%). The choice of 1,4-dioxane is for its density being close to that of water.

Microfluidics

The microfluidic experiment was conducted in a coaxial mixer. Two capillaries were coaxially aligned: a cylindrical silica capillary (*TSP020090*, *Molex*, inner diameter 20 µm, outer diameter 90 µm) inside a cylindrical borosilicate tube (*CV2033*, *Vitrocom*, inner diameter 200 µm, outer diameter 330 µm) through a PEEK (polyether ether ketone) 7-port manifold (*P170*, *IDEX*). The microfluidic system was mounted on a 3D printed (*Designjet*, *HP*) holder made from ABS (acrylonitrile butadiene styrene). The solution of DBDCS in 1,4-dioxane was injected through the small central capillary into a peripheral flow of a cosolvent mixture. The flow rates were independently controlled: the central flow with a *Pico Plus Elite* syringe pump (*Harvard Apparatus*) and the peripheral flow with a *PHD2000* syringe pump (*Harvard Apparatus*).

Optical microscopy

The phase transitions were observed using a home-modified two-turret inverted microscope (*TE2000-U*, *Nikon)*. The objective used was a *CFI S Plan Fluor ELWD* (*Nikon*, working distance 8.2 to 6.9 mm, magnification 20×, numerical aperture 0.45, infinite corrected, correction ring range 0 to 2.6 mm). A parfocal length extender ring of 5 mm thickness was added to match the appropriate focusing distance at the sample plane. Image acquisition was performed using a CCD (charge-coupled device) camera (*Retiga R1*, *Teledyne Qimaging*, pixel size 6.45 µm), controlled through *µManager* open-source software.

Fluorescence

The fluorescence was observed through the above-mentioned microscope. The excitation beam was the third harmonic generation (LBO, *EKSMA Optics*, wavelength 1030→343 nm) of a mode-locked Yb:KYW infrared laser (*t-Pulse 200*, *Amplitude System*, wavelength 1030 nm, pulse 400 fs at full width at half maximum, repetition rate 10 MHz, average power 2.7 W). A UV dichroic mirror (reflectance > 95% at wavelength 330-340 nm) was used to excite the sample. A 300mm focal lens tube was used in combination with the objective to achieve the wide-field illumination. The fluorescence emission passed through a 514 nm notch filter (*NF03-514E-25*, *Semrock*, optical density 5 at 343 nm) and a 785 nm short-pass filter (*BSP01-785R-25*, *Semrock*, optical density 7 at 1030 nm). A time-and-space-resolved single photon detector (*LINCam*, *Photonscore*, spatial resolution 40 μm on the photocathode chip, instrumental response function 50 ps, digitalized image size 4096×4096 pixels) was used to record the emitted photons with their locations on the photocathode, their absolute arrival time, and their arrival time with respect to the pulse laser excitation. The photon acquisition was controlled through *LnTCapture* software (*Photonscore*).

Associated content

Supporting Information

Chemical potentials in water-[1,4-dioxane]-DBDCS; Properties of water, 1,4-dioxane, and DBDCS; Density of water-[1,4-dioxane]; Dynamic viscosity of water-[1,4-dioxane]; Thermodynamic factor of water-[1,4-dioxane]; Maxwell-Stefan diffusivity of water-[1,4-dioxane]; Self-diffusion coefficient of DBDCS in water-[1,4-dioxane]; Structure of the coaxial flow; Diffusion simulation coupled with hydrodynamics; Evolution of profiles of water and 1,4-dioxane; Phase diagram of water-[1,4-dioxane]-DBDCS; Energy of composition fluctuation; Sites for antisolvent-induced spinodal decomposition; Solute downhill diffusion without antisolvent; Parallelism in diffusion trajectories (PDF)

Video 1

Time-dependent simulation of antisolvent-induced uphill diffusion followed by downhill diffusion of DBDCS in water-[1,4-dioxane], with initial solute concentration in **R**, $\rho_{3\mathrm{R}} = 8.8\,\mathrm{g/L}$, initial antisolvent volume fraction in **L**, $\phi_{1\mathrm{L}} = 80\%$, antisolvent-to-solution size ratio, **L**/**R**=1/1, and no convection (GIF)

Video 2

Time-dependent simulation of antisolvent-induced spinodal decomposition of DBDCS in water-[1,4-dioxane], with initial solute concentration in **R**, $\rho_{3\mathrm{R}} = 9\,\mathrm{g/L}$, initial antisolvent volume fraction in **L**, $\phi_{1\mathrm{L}} = 80\%$, antisolvent-to-solution size ratio, **L**/**R**=1/1, and no convection (GIF)

Author information

Corresponding author

Zhengyu Zhang – Université Paris-Saclay, CNRS, Ecole Normale Supérieure Paris-Saclay, CentraleSupélec, Laboratoire LuMIn, 91190 Gif-sur-Yvette, France; Université Paris-Saclay, CentraleSupélec, CNRS, Laboratoire SPMS, 91190 Gif-sur-Yvette,

France; Université Paris Saclay, Institut d'Alembert (IDA), CNRS, Ecole Normale Supérieure Paris-Saclay, 91190 Gif-sur-Yvette, France; orcid.org/0000-0002-1254-6225

*E-mail: zhengyu.zhang@centralesupelec.fr

Authors

Jean-Frédéric Audibert – Université Paris-Saclay, CNRS, Ecole Normale Supérieure Paris-Saclay, Laboratoire PPSM, 91190 Gif-sur-Yvette, France; Université Paris Saclay, Institut d'Alembert (IDA), CNRS, Ecole Normale Supérieure Paris-Saclay, 91190 Gif-sur-Yvette, France; orcid.org/0000-0002-2511-3111; jaudiber@ppsm.ens-cachan.fr;

Weixi Wang – École polytechnique, LPICM, CNRS, Institut Polytechnique de Paris, 91120 Palaiseau, France; orcid.org/0009-0004-9869-0149; weixi.wang@polytechnique.edu

Valérie Génot – IUT d'Orsay, Université Paris Saclay, 91190 Gif-sur-Yvette, France; valerie.genot@universite-paris-saclay.fr

Soo Young Park – Department of Materials Science and Engineering, Seoul National University, 1 Gwanak-ro, Gwanak-gu, Seoul 151-744, Korea; orcid.org/0000-0002-2272-8524; parksy@snu.ac.kr

Anne Spasojević-de Biré – Université Paris-Saclay, CentraleSupélec, CNRS, Laboratoire SPMS, 91190 Gif-sur-Yvette, France; orcid.org/0000-0003-3819-3197; anne.spasojevic@centralesupelec.fr

Robert B. Pansu – Université Paris-Saclay, CNRS, Ecole Normale Supérieure Paris-Saclay, CentraleSupélec, Laboratoire LuMIn, 91190 Gif-sur-Yvette, France; Université Paris Saclay, Institut d'Alembert (IDA), CNRS, Ecole Normale

Supérieure Paris-Saclay, 91190 Gif-sur-Yvette, France; orcid.org/0000-0002-5588-3950; pansu@ens-paris-saclay.fr

Author contributions

Z.Z.: Conceptualization, Methodology, Formal analysis, Investigation, Resources, Data Curation, Writing - Original Draft, Writing - Review & Editing, Visualization. **J.-F.A.**: Methodology, Formal analysis, Investigation, Resources, Writing - Original Draft. **W.W.**: Validation, Investigation, Writing - Review & Editing, Visualization. **V.G.** Methodology, Investigation. **S.Y.P.**: Resources. **A.S.-d.B.**: Methodology, Investigation, Writing - Review & Editing, Supervision, Project administration, Funding acquisition. **R.B.P.**: Conceptualization, Methodology, Validation, Formal analysis, Investigation, Resources, Writing - Original Draft, Writing - Review & Editing, Supervision, Project administration, Funding acquisition.

Declaration of competing interest

The authors declare no competing financial interest.

Data availability

All data that support the plots within this paper are available from the corresponding author upon reasonable request.

Acknowledgement

This work received support from le Laboratoire d'Excellence (LabEx) CHARMMMAT [grant number ANR-11-IDEX-0003-02], l'école doctorale INTERFACES (ED 573), and l'Agence Nationale de la Recherche (ANR) [SUCRINE project, grant number ANR-22-CE51-0023]. Some elements (the crystals and droplets growing in the beaker) of the TOC graphic were generated using *DALL·E 3*, *OpenAI*'s text to image model.

References

(1) L'vov, P. E.; Umantsev, A. R. Two-Step Mechanism of Macromolecular Nucleation and Crystallization: Field Theory and Simulations. *Crystal Growth & Design* **2021**, *21* (1), 366-382. DOI: 10.1021/acs.cgd.0c01224.

(2) Zhang, Z.; Bi, R.; Audibert, J.-F.; Wang, W.; Park, S. Y.; Spasojević-de Biré, A.; Pansu, R. B. Thermodynamics of Oiling-Out in Antisolvent Crystallization. I. Extrapolation of Ternary Phase Diagram from Solubility to Instability. *Crystal Growth & Design* **2024**, *24* (1), 224-237. DOI: 10.1021/acs.cgd.3c00916.

(3) Takasuga, M.; Ooshima, H. Control of Crystal Aspect Ratio and Size by Changing Solvent Composition in Oiling Out Crystallization of an Active Pharmaceutical Ingredient. *Crystal Growth & Design* **2015**, *15* (12), 5834-5838. DOI: 10.1021/acs.cgd.5b01192.

(4) Sun, M.; Du, S.; Chen, M.; Rohani, S.; Zhang, H.; Liu, Y.; Sun, P.; Wang, Y.; Shi, P.; Xu, S.; et al. Oiling-Out Investigation and Morphology Control of β-Alanine Based on Ternary Phase Diagrams. *Crystal Growth & Design* **2018**, *18* (2), 818-826. DOI: 10.1021/acs.cgd.7b01293.

(5) Vitale, S. A.; Katz, J. L. Liquid Droplet Dispersions Formed by Homogeneous Liquid−Liquid Nucleation: "The Ouzo Effect". *Langmuir* **2003**, *19* (10), 4105-4110. DOI: 10.1021/la026842o.

(6) Solans, C.; Morales, D.; Homs, M. Spontaneous emulsification. *Current Opinion in Colloid & Interface Science* **2016**, *22*, 88-93. DOI: 10.1016/j.cocis.2016.03.002.

(7) Sitnikova, N. L.; Sprik, R.; Wegdam, G.; Eiser, E. Spontaneously formed trans-anethol/water/alcohol emulsions: mechanism of formation and stability. *Langmuir* **2005**, *21* (16), 7083-7089. DOI: 10.1021/la046816l.

(8) Krishna, R. Serpentine diffusion trajectories and the Ouzo effect in partially miscible ternary liquid mixtures. *Phys Chem Chem Phys* **2015**, *17* (41), 27428-27436. DOI: 10.1039/c5cp04520g.

(9) Krishna, R. Diffusing uphill with James Clerk Maxwell and Josef Stefan. *Chemical Engineering Science* **2019**, *195*, 851-880. DOI: 10.1016/j.ces.2018.10.032.

(10) Thorat, A. A.; Dalvi, S. V. Liquid antisolvent precipitation and stabilization of nanoparticles of poorly water soluble drugs in aqueous suspensions: Recent developments and future perspective. *Chemical Engineering Journal* **2012**, *181-182*, 1-34. DOI: 10.1016/j.cej.2011.12.044.

(11) Jiang, S.; ter Horst, J. H.; Jansens, P. J. Concomitant Polymorphism ofo-Aminobenzoic Acid in Antisolvent Crystallization. *Crystal Growth & Design* **2008**, *8* (1), 37-43. DOI: 10.1021/cg070517n.

(12) Punmalee, N.; Wantha, L.; Flood, A. E. Antisolvent Crystallization of Polymorphs of L-Histidine. *Chemical Engineering & Technology* **2018**, *41* (6), 1132-1138. DOI: 10.1002/ceat.201700676.

(13) Zhao, H.; Xie, C.; Xu, Z.; Wang, Y.; Bian, L.; Chen, Z.; Hao, H. Solution Crystallization of Vanillin in the Presence of a Liquid–Liquid Phase Separation. *Industrial & Engineering Chemistry Research* **2012**, *51* (45), 14646-14652. DOI: 10.1021/ie302360u.

(14) Parimaladevi, P.; Supriya, S.; Srinivasan, K. The role of ultrasound in controlling the liquid-liquid phase separation and nucleation of vanillin polymorphs I and II. *Journal of Crystal Growth* **2018**, *484*, 21-30. DOI: 10.1016/j.jcrysgro.2017.12.023.

(15) Thorson, M. R.; Goyal, S.; Gong, Y.; Zhang, G. G. Z.; Kenis, P. J. A. Microfluidic approach to polymorph screening through antisolvent crystallization. *CrystEngComm* **2012**, *14* (7), 2404-2412, 10.1039/C2CE06167H. DOI: 10.1039/c2ce06167h.

(16) Jia, S.; Yang, P.; Gao, Z.; Li, Z.; Fang, C.; Gong, J. Recent progress in antisolvent crystallization. *CrystEngComm* **2022**, *24* (17), 3122-3135, 10.1039/D2CE00059H. DOI: 10.1039/D2CE00059H.

(17) Supriya, S.; Sushmitha, S.; Srinivasan, K. Effective Control of Liquid–Liquid Phase Separation and Nucleation of Vanillin Single Crystals through a Vapor Diffusion Crystallization Process in Selected Solvent Environments. *Crystal Growth & Design* **2019**, *19* (11), 6315-6323. DOI: 10.1021/acs.cgd.9b00798.

(18) Tanaka, K.; Takiyama, H. Effect of Oiling-Out during Crystallization on Purification of an Intermediate Compound. *Organic Process Research & Development* **2019**, *23* (9), 2001-2008. DOI: 10.1021/acs.oprd.9b00256.

(19) Maier, R.; Zocher, G.; Sauter, A.; Da Vela, S.; Matsarskaia, O.; Schweins, R.; Sztucki, M.; Zhang, F.; Stehle, T.; Schreiber, F. Protein Crystallization in the Presence of a Metastable Liquid–Liquid Phase Separation. *Crystal Growth & Design* **2020**, *20* (12), 7951-7962. DOI: 10.1021/acs.cgd.0c01219.

(20) Zhang, Z. Laser-Induced Nucleation in a Coaxial Microfluidic Mixer. Université Paris Saclay (COmUE), Gif-sur-Yvette, Essonne, 2019, http://www.theses.fr/2019SACLN023.

(21) Miller, R.; Sefcik, J.; Lue, L. Modeling Diffusive Mixing in Antisolvent Crystallization. *Crystal Growth & Design* **2022**, *22* (4), 2192-2207. DOI: 10.1021/acs.cgd.1c01269.

(22) Yoon, S. J.; Chung, J. W.; Gierschner, J.; Kim, K. S.; Choi, M. G.; Kim, D.; Park, S. Y. Multistimuli two-color luminescence switching via different slip-stacking of highly fluorescent molecular sheets. *J Am Chem Soc* **2010**, *132* (39), 13675-13683. DOI: 10.1021/ja1044665.

(23) Álvarez-Asencio, R.; Moreno-Ramírez, J. S.; Pimentel, C.; Casado, S.; Matta, M.; Gierschner, J.; Muccioli, L.; Yoon, S.-J.; Varghese, S.; Park, S. Y.; et al. Molecular-scale shear response of the organic semiconductor β-DBDCS (100) surface. *Physical Review B* **2017**, *96* (11), 115422. DOI: 10.1103/PhysRevB.96.115422.

(24) Tran, V. L.; Génot, V.; Audibert, J.-F.; Prokazov, Y.; Turbin, E.; Zuschratter, W.; Kim, H.-J.; Jung, J.; Park, S. Y.; Pansu, R. B. Nucleation and growth during a fluorogenic precipitation in a micro-flow mapped by fluorescence lifetime microscopy. *New Journal of Chemistry* **2016**, *40* (5), 4601-4605. DOI: 10.1039/c5nj03400k.

(25) Acree, W. E. Mathematical representation of thermodynamic properties. *Thermochimica Acta* **1992**, *198* (1), 71-79. DOI: 10.1016/0040-6031(92)85059-5.

(26) Jouyban, A.; Acree, W. E. Mathematical derivation of the Jouyban-Acree model to represent solute solubility data in mixed solvents at various temperatures. *Journal of Molecular Liquids* **2018**, *256*, 541-547. DOI: 10.1016/j.molliq.2018.01.171.

(27) Taylor, R.; Krishna, R. *Multicomponent mass transfer*; John Wiley & Sons, 1993.

(28) Maxwell, J. C. IV. On the dynamical theory of gases. *Philosophical Transactions of the Royal Society of London* **1866**, *157*, 49-88. DOI: 10.1098/rstl.1867.0004.

(29) Fick, A. V. On liquid diffusion. *The London, Edinburgh, and Dublin Philosophical Magazine and Journal of Science* **1855**, *10* (63), 30-39. DOI: 10.1080/14786445508641925.

(30) Stefan, J. Über das Gleichgewicht und die Bewegung, insbesondere die Diffusion von Gasgemengen. *Sitzungsberichte der Mathematisch-Naturwissenschaftlichen Classe der Kaiserlichen Akademie der Wissenschaften Wien, 2te Abteilung* **1871**, *63*, 63-124.

(31) Onsager, L. Reciprocal Relations in Irreversible Processes. I. *Physical Review* **1931**, *37* (4), 405-426. DOI: 10.1103/PhysRev.37.405.

(32) Onsager, L. Reciprocal Relations in Irreversible Processes. II. *Physical Review* **1931**, *38* (12), 2265-2279. DOI: 10.1103/PhysRev.38.2265.

(33) Onsager, L. Theories and problems of liquid diffusion. *Ann N Y Acad Sci* **1945**, *46* (5), 241-265. DOI: 10.1111/j.1749-6632.1945.tb36170.x.

(34) Standart, G. L.; Taylor, R.; Krishna, R. THE MAXWELL-STEFAN FORMULATION OF IRREVERSIBLE THERMODYNAMICS FOR SIMULTANEOUS HEAT AND MASS TRANSFER. *Chemical Engineering Communications* **1979**, *3* (4-5), 277-289. DOI: 10.1080/00986447908935866.

(35) Curtiss, C. F.; Bird, R. B. Multicomponent Diffusion. *Industrial & Engineering Chemistry Research* **1999**, *38* (7), 2515-2522. DOI: 10.1021/ie9901123.

(36) Bird, R. B.; Lightfoot, E. N.; Stewart, W. E. *Transport Phenomena*; J. Wiley, 2002.

(37) Truesdell, C.; Toupin, R. The Classical Field Theories. In *Principles of Classical Mechanics and Field Theory / Prinzipien der Klassischen Mechanik und Feldtheorie*, Flügge, S. Ed.; Springer Berlin Heidelberg, 1960; pp 226-858. DOI: 10.1007/978-3-642-45943-6_2.

(38) Landi, G. T.; Paternostro, M. Irreversible entropy production: From classical to quantum. *Reviews of Modern Physics* **2021**, *93* (3), 035008. DOI: 10.1103/RevModPhys.93.035008.

(39) Stokes, G. G. On the Effect of the Internal Friction of Fluids on the Motion of Pendulums. *Transactions of the Cambridge Philosophical Society* **1851**, *9, Part II*, 8-106.

(40) Navier, C. L. M. H. Mémoire sur les lois du mouvement des fluides (lu à l'Académie royale des sciences le 18 mars 1822). *Mémoires de l'Académie des sciences* **1827**, *6*, 389-440. https://fr.wikisource.org/wiki/M%C3%A9moire_sur_les_lois_du_mouvement_des_fluides#.

(41) Stokes, G. G. On the Theories of the Internal Friction of Fluids in Motion, and of the Equilibrium and Motion of Elastic Solids. *Transactions of the Cambridge Philosophical Society* **1845**, *8*, 287-319. From Cambridge University Press Cambridge Core.

(42) Einstein, A. Über die von der molekularkinetischen Theorie der Wärme geforderte Bewegung von in ruhenden Flüssigkeiten suspendierten Teilchen. *Annalen der Physik* **1905**, *322* (8), 549-560. DOI: 10.1002/andp.19053220806.

(43) Perrin, J. Mouvement brownien et molécules. *J. Phys. Theor. Appl.* **1910**, *9* (1), 5-39. DOI: 10.1051/jphystap:0191000900500 Ajp.

(44) Krishna, R.; van Baten, J. M. The Darken Relation for Multicomponent Diffusion in Liquid Mixtures of Linear Alkanes: An Investigation Using Molecular Dynamics (MD) Simulations. *Industrial & Engineering Chemistry Research* **2005**, *44* (17), 6939-6947. DOI: 10.1021/ie050146c.

(45) Liu, X.; Vlugt, T. J. H.; Bardow, A. Maxwell–Stefan diffusivities in liquid mixtures: Using molecular dynamics for testing model predictions. *Fluid Phase Equilibria* **2011**, *301* (1), 110-117. DOI: 10.1016/j.fluid.2010.11.019.

(46) Higashi, H.; Tamura, K.; Seto, T.; Otani, Y. Direct calculation of mutual diffusion coefficients of binary system using non-equilibrium molecular dynamics simulation. *Fluid Phase Equilibria* **2015**, *402*, 83-88. DOI: 10.1016/j.fluid.2015.05.029.

(47) Janzen, T.; Vrabec, J. Diffusion Coefficients of a Highly Nonideal Ternary Liquid Mixture: Cyclohexane–Toluene–Methanol. *Industrial & Engineering Chemistry Research* **2018**, *57* (48), 16508-16517. DOI: 10.1021/acs.iecr.8b04385.

(48) Liu, X.; Vlugt, T. J. H.; Bardow, A. Predictive Darken Equation for Maxwell-Stefan Diffusivities in Multicomponent Mixtures. *Industrial & Engineering Chemistry Research* **2011**, *50* (17), 10350-10358. DOI: 10.1021/ie201008a.

(49) Allie-Ebrahim, T.; Zhu, Q.; Brauer, P.; Moggridge, G. D.; D'Agostino, C. Maxwell-Stefan diffusion coefficient estimation for ternary systems: an ideal ternary alcohol system. *Phys Chem Chem Phys* **2017**, *19* (24), 16071-16077, 10.1039/C7CP02582C. DOI: 10.1039/c7cp02582c.

(50) Allie-Ebrahim, T.; Russo, V.; Ortona, O.; Paduano, L.; Tesser, R.; Di Serio, M.; Singh, P.; Zhu, Q.; Moggridge, G. D.; D'Agostino, C. A predictive model for the diffusion of a highly non-ideal ternary system. *Phys Chem Chem Phys* **2018**, *20* (27), 18436-18446, 10.1039/C8CP03227K. DOI: 10.1039/c8cp03227k.

(51) Darken, L. S. Diffusion, mobility and their interrelation through free energy in binary metallic systems. *Trans. Aime* **1948**, *175*, 184-201.

(52) Vignes, A. Diffusion in Binary Solutions. Variation of Diffusion Coefficient with Composition. *Industrial & Engineering Chemistry Fundamentals* **1966**, *5* (2), 189-199. DOI: 10.1021/i160018a007.

(53) Wesselingh, J. A.; Bollen, A. M. Multicomponent Diffusivities from the Free Volume Theory. *Chemical Engineering Research and Design* **1997**, *75* (6), 590-602. DOI: 10.1205/026387697524119.

(54) Zhu, Q.; D'Agostino, C.; Ainte, M.; Mantle, M. D.; Gladden, L. F.; Ortona, O.; Paduano, L.; Ciccarelli, D.; Moggridge, G. D. Prediction of mutual diffusion coefficients in binary liquid systems with one self-associating component from viscosity data and intra-diffusion coefficients at infinite dilution. *Chemical Engineering Science* **2016**, *147*, 118-127. DOI: 10.1016/j.ces.2016.03.020.

(55) self-diffusion coefficient. 3.0.1 ed.; International Union of Pure and Applied Chemistry (IUPAC), 2019. DOI: doi:10.1351/goldbook.S05582.

(56) Van Ness, H. Classical thermodynamics of non-electrolyte solutions. **1964**.

(57) Sutherland, W. LXXV. A dynamical theory of diffusion for non-electrolytes and the molecular mass of albumin. *The London, Edinburgh, and Dublin Philosophical Magazine and Journal of Science* **1905**, *9* (54), 781-785. DOI: 10.1080/14786440509463331.

(58) Cahn, J. W.; Hilliard, J. E. Free Energy of a Nonuniform System. III. Nucleation in a Two‐Component Incompressible Fluid. *The Journal of Chemical Physics* **1959**, *31* (3), 688-699. DOI: 10.1063/1.1730447 (acccessed 2022/03/04).

(59) Cahn, J. W.; Hilliard, J. E. Free Energy of a Nonuniform System. I. Interfacial Free Energy. *The Journal of Chemical Physics* **1958**, *28* (2), 258-267. DOI: 10.1063/1.1744102.

(60) Cahn, J. W. Theory of crystal growth and interface motion in crystalline materials. *Acta Metallurgica* **1960**, *8* (8), 554-562. DOI: 10.1016/0001-6160(60)90110-3.

(61) Cahn, J. W. On spinodal decomposition. *Acta Metallurgica* **1961**, *9* (9), 795-801. DOI: 10.1016/0001-6160(61)90182-1.

(62) Zanella, R.; Tellier, R. L.; Plapp, M.; Tegze, G.; Henry, H. Three-dimensional numerical simulation of droplet formation by Rayleigh–Taylor instability in multiphase corium. *Nuclear Engineering and Design* **2021**, *379*, 111177. DOI: https://doi.org/10.1016/j.nucengdes.2021.111177.

(63) Hajian, R.; Hardt, S. Formation and lateral migration of nanodroplets via solvent shifting in a microfluidic device. *Microfluidics and Nanofluidics* **2015**, *19* (6), 1281-1296, journal article. DOI: 10.1007/s10404-015-1644-7.